TECHNISCHE
UNIVERSITÄT
WIEN

INSTITUT FÜR PHOTONIK
Photonics Institute

DIPLOMARBEIT

Multi-millijoule femtosecond laser pulse bursts

zur Erlangung des akademischen Grades

Diplom-Ingenieur

im Rahmen des Studiums

Mikroelektronik und Photonik

eingereicht von

Vinzenz Stummer
Matrikelnummer 01125138

ausgeführt am Institut für Photonik
der Fakultät für Elektrotechnik und Informationstechnik der Technischen Universität Wien

Betreuung
Hauptbetreuung: Univ. Prof. PhD Andrius Baltuška
Mitbetreuung: Dipl.-Ing. Tobias Flöry

Wien, 20.09.2019

(Unterschrift Verfasser)

(Unterschrift Betreuer)

Acknowledgments

I would like to express my gratitude to Andrius Baltuška for giving me the opportunity to work on a fascinating project, in which I could contribute in the course of this thesis in various ways.
A lot of thanks also goes to Tobias Flöry for introducing me to the laboratory setup, teaching me many interesting things and for being an excellent collaborator.
Finally, I would like to thank my family for supporting me in every possible way.

Contents

1 Introduction

The generation and control of ultrashort laser pulses started a huge field of research [1] and ever since, technology in this field developed further [2]. One of these is the generation of femtosecond (fs) laser pulse bursts: This means the generation of pulse bursts, which consist of pulses with a several magnitudes shorter temporal spacing compared to the burst repetition time. In the past, usual methods for generating fs pulse bursts were developed like picking pulses from the pulse train of a master oscillator [3–5], using linear, time-invariant spectral filters [6–18] or nonlinear methods [19]. However, none of these methods satisfy the needs for fully tunable control of all burst parameters over a wide range, like intraburst frequency, burst energy, number of pulses or individual intraburst pulse parameters such as pulse peak intensities or intraburst CEPs.

Methods based on the Vernier effect, which utilize two cavities detuned in round-trip time together with a pulse accumulation mechanism, enable burst generation with a high scalability of the number of pulses in the burst and a tunable pulse spacing down to the sub-picosecond regime, corresponding to THz intraburst frequencies, exceeding the limits given by state-of-the-art methods by several orders of magnitude. Very recently, a new approach for the generation of fs pulse bursts, based on the Vernier effect, was invented [20]: It comprises a regenerative amplifier, whose cavity round-trip time is slightly detuned to that of the master oscillator and a Pockels Cell voltage protocol as pulse accumulation mechanism in the regenerative amplifier.

However, there is still room for further development of the mentioned approach. Implementation of an optical modulator, like an acousto-optical modulator, between the detuned cavities, allows control of individual pulse parameters. The focus in this work is especially on the control and stabilization of individual intraburst CEPs, which enables the generation of reproducible fs pulse bursts and a high amplification of bursts with sub-ps pulse spacing in optical amplifiers when using Chirped Pulse Amplification (CPA), giving access to the multi-millijoule regime. Thus, generation and strong amplification of fs pulse bursts with unprecedented properties and control will be demonstrated. This will be further motivated by proposing several potential applications of the generated bursts.

This thesis is structured as following: In chapter 2, a definition of fs pulse bursts together with a presentation of relevant physical properties regarding the technical utilization of bursts is given (Sec. 2.1), followed by a discussion of state-of-the-art methods for the generation of fs pulse bursts (Sec. 2.2), including an introduction to burst generation using the Vernier effect (Sec. 2.2.4). Chapter 3 deals with further development of Vernier methods realized in course of this thesis in the laboratory: The amplification of fs pulse bursts up to the multi-millijoule regime and its technical requirements (Sec. 3.4) and the stabilization of intraburst CEP drift (Sec. 3.5). Subject of chapter 4 are potential applications of the generated bursts, like materials processing (Sec. 4.1), THz-generation (Sec. 4.2), nonlinear spectroscopy (Sec. 4.3) and a technique for quantum control (Sec. 4.4). Finally, a pulse broadening mechanism arising during the generation of continuously-tunable, narrowband THz pulses is investigated in detail in chapter 5, both theoretically and experimentally, leading to a deeper understanding of the THz-generation process and motivating the stabilization of intraburst CEPs.

2 Femtosecond pulse burst generation

First of all, a definition of femtosecond (fs) laser pulse bursts and their physical parameters is given (Sec. 2.1). Then, different concepts of burst generation are presented and discussed in greater detail each, together with realization examples (Sec. 2.2). Afterwards, the advantages and drawbacks of current burst generations methods are discussed (Sec. 2.3).

2.1 Definition of fs laser pulse bursts

In general, a fs laser pulse burst can be defined as a train of fs laser pulses with very short temporal pulse spacing Δt. Since usually not a single burst is generated, the term "very short" means practically, that it is orders of magnitudes shorter compared to the spacing between bursts, given by the inverse repetition rate $1/f_{rep}$ of bursts. Physical parameters of a burst are depicted in Fig. 2.1 and listed in Tab. 2.1. Mentionable are the intraburst repetition rate f_{burst} and intraburst carrier-to-envelope phase (CEP) $\phi_{ij} = \phi_i - \phi_j$: The former arises from the temporal pulse spacing and is a fundamental parameter for THz-generation with fs pulse bursts (Sec. 5) and the latter corresponds to the relative CEPs of the pulses in the burst, which will be an important property for most of the results in this thesis. As shown in Tab. 2.1, the intraburst CEP can be arbitrarily defined to be relative to the phase of the first pulse $\phi_{i1} = \phi_i - \phi_1$, though any other pulse in the burst can also provide the reference phase.

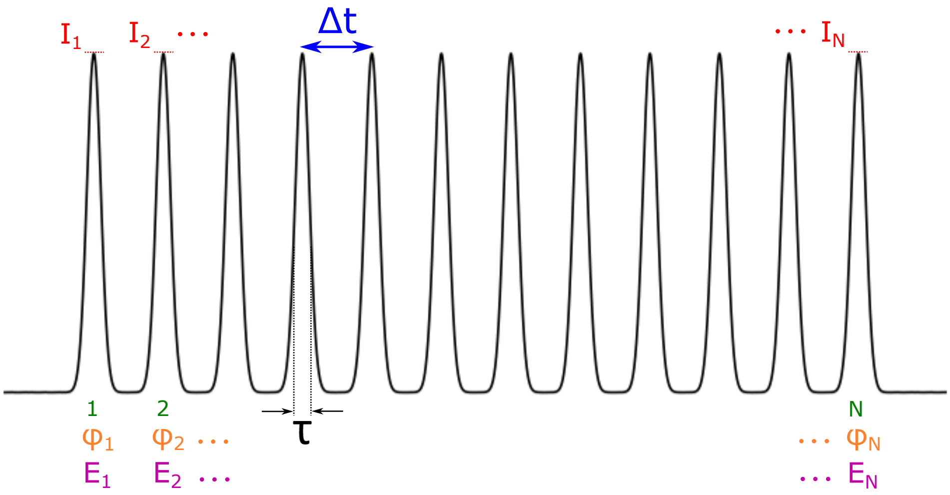

Figure 2.1: Definition of physical parameters of a pulse burst

τ	pulse length
Δt	temporal pulse spacing
f_{rep}	burst repetition rate
$f_{burst} = 1/\Delta t$	intraburst repetition rate
N	number of pulses
$I_{preak,i}$	peak intensities
E_i	pulse energies
ϕ_i	CEP
$\phi_{i1} = \phi_i - \phi_1$	intraburst CEP

Table 2.1: Physical parameters of a pulse burst

For currently established methods (Sec. 2.2), a lot of parameter ranges concurrent with each other, for example when generating bursts with very short pulse length ($\approx 10fs$), short pulse spacing ($\approx 10ps$) and millijoule pulse energies, due to the reasons described in Sec. 3.1.

2.2 Methods of fs pulse burst generation

An enormous variety of pulse burst generation methods was realized, where every form of burst generation can generally be associated with one of four different concepts:

- Pulse picking: Pulses are picked out from a master oscillator pulse train or from a single pulse circulating in a cavity (Sec. 2.2.1).
- Linear, time-invariant spectral filters: By applying a periodic spectral filter, the spectral amplitude and phase of a pulse can be modulated in such a way, that a burst in the time-domain is formed (Sec. 2.2.2). This can be realized for example by time-space-conversion, by using Arrayed-Waveguide Gratings (AWG), Fiber Diffraction Gratings (FDG), coupled-cavities or by utilizing birefringence.
- Nonlinear methods: Pulse bursts can be formed from single fs pulses by utilizing the interplay between nonlinearities and dispersion. This is explained further in Sec. 2.2.3.
- Vernier effect: A pulsed laser master oscillator is combined with a second cavity (which can be completely passive, or the cavity of an amplifier), whose round-trip time is detuned by the master oscillator round-trip time. Together with a mechanism for pulse accumulation in the second cavity, this leads to the formation of bursts with a pulse spacing corresponding to the cavity detuning (Sec. 2.2.4).

2.2.1 Pulse picker

The principle of a pulse picker is to select specific pulses from a master oscillator pulse train by using either one sampling window, which selects N consecutive pulses from the oscillator, or several sampling windows selecting every nth pulse, thus setting the intraburst repetition rate f_{burst} to $1/n$ of the oscillator repetition rate f_{osc}. The sampling window can be realized by using either electro-optic switches, like a pair of Pockels cells (PC) [3, 4] or an acousto-optic modulator (AOM) [5], where the latter spares expensive fast, high-voltage electronics and thus is a much more economical approach with comparable performance.

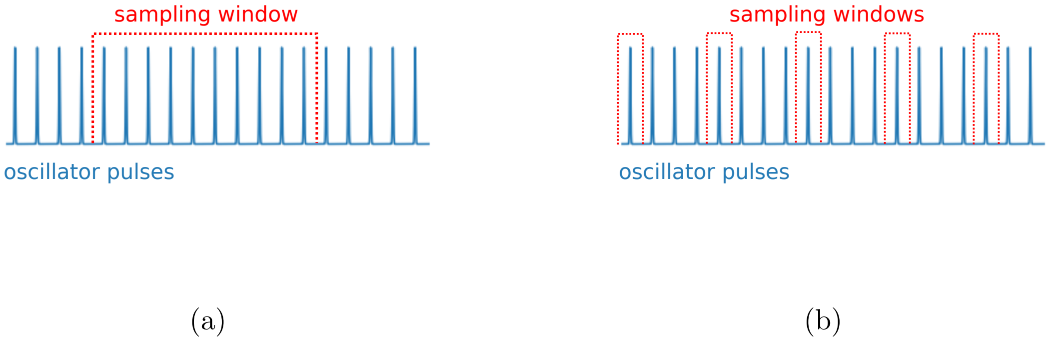

(a) (b)

Figure 2.2: Generation of pulse bursts by selecting pulses from the master oscillator by using a) a single window giving $f_{burst} = f_{osc}$ b) multiple sampling windows selecting every n pulse, thus giving $f_{burst} = f_{osc}/n$.

The intraburst repetition rate of a burst generated this way is limited to the oscillator repetition rate f_{osc}, which is usually in the MHz range, leading to an intraburst pulse spacing Δt in the ns-regime. Also, the intraburst repetition rate f_{burst} is not continuously tunable, since it is limited to f_{osc}/n. However, the scalability of pulses is very high, since the sampling window can be set to an arbitrary length.

The pulse picker can also be implemented as an electro-optic switch in a cavity with a pulse circulating in it. By making the cavity partially transparent, it is possible to couple out the circulating pulse in the cavity over several round-trips [21]. The generated burst has a pulse spacing equal to the cavity round-trip time. If a regenerative amplifier (RA) is used as cavity, the scalability of pulses is given by setting the amplification before coupling out the pulse and by adjusting the level of transparency of the cavity. Therefore, the intracavity pulse picker has similar properties as the extracavity pulse picker regarding output burst properties.

2.2.2 Linear, time-invariant spectral filters

As known from linear, time-invariant filtering, the modulation of a signal in the time-domain $x(t)$ can be described by the action of a filter $h(t)$ as

$$y(t) = (h * x)(t) = \int_{-\infty}^{+\infty} h(t-\tau)x(\tau)d\tau, \tag{2.1}$$

which corresponds to a following relationship of the respective Fourier-transforms $H(\omega)$, $X(\omega)$ and $Y(\omega)$:

$$Y(\omega) = H(\omega) \cdot X(\omega). \tag{2.2}$$

Thus, spectral amplitude- and/or phase-filters can be utilized for burst formation in the time-domain by using Fourier-transform relationships. The burst can be tailored by the design of the filter, which allows generation of bursts with pulse spacings down to picoseconds. In case of the SLM (Sec. 2.2.2) the pulse spacing is even tunable discretely. The number of pulses and the tunable range of the pulse spacing is limited by the spectral resolution of the filter. Besides, design goals where currently mostly restricted to pulse spacing, pulse length and peak intensities (mostly flat-topped for telecommunication applications), but not to intraburst CEP. Also the tuning of individual intraburst pulse parameters is limited compared to other methods like pulse slicing or Vernier methods. Generally, there are two ways to use linear spectral filters for burst formation, which will be explained in the following, and for both ways a spectrally periodic filter is needed, whose spectral period is called the Free Spectral Range (FSR):

Pulse Repetition Rate Multiplication (PRRM)

The first way is Pulse Repetition Rate Multiplication (PRRM) (Fig. 2.3) and can be explained followingly:
A linear spectral filter has the capability of multiplying the repetition rate f_{train} of a pulse train by a factor of N_{PRRM}, if the FSR satisfies the condition

$$\frac{FSR}{f_{train}} = \frac{N_{PRRM}}{D}, \tag{2.3}$$

with D and N_{PRRM} both being integers and $\frac{N_{PRRM}}{D}$ an irreducible rational number, as it is shown in [6]. In Fig. 2.3a, this can be seen for $D = 1$ and $N_{PRRM} = 3$. It is important to notice, that there is for a given multiplication factor N_{PRRM} some freedom to choose the FSR for a filter design, since D can also be larger than 1. However, the repetition rate cannot be set arbitrarily high, because of the limited single pulse bandwidth (BW) as can be seen in Fig. 2.3b. In the time-domain this can be understood as that the pulse spacing should not be decreased so far, such that pulses start overlapping. In the end, a burst with a higher intraburst repetition rate $f_{burst} = N_{PRRM} \cdot f_{train}$ compared to the original train repetition rate f_{train} can be formed by pulse picking the filtered pulse train. The formation of a burst by pulse picking allows for high subsequent amplification of the pulses, sustaining the high intraburst frequency, while keeping the average power low and thus, omitting the saturation of amplifiers.

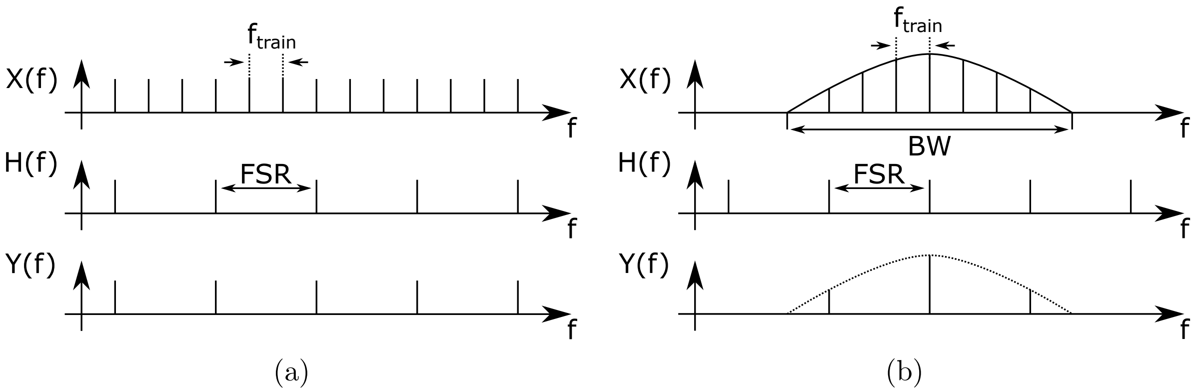

Figure 2.3: PRRM with a linear, time-invariant filter with spectral periodicity FSR and (a) infinite single pulse bandwidth (b) finite single pulse bandwidth

Direct burst generation

A burst can also be directly generated from a low repetition rate source with a spectrally periodic filter. The burst repetition rate f_{rep} is then equal to the repetition rate of the original pulse train f_{train} and the intraburst repetition rate is equal to the FSR of the filter. Note, that the FSR must not be higher than the single pulse bandwidth, as mentioned above. Overall, this is an elegant approach, since the burst generation can be completely reduced to the action of a suitably designed filter, regardless of the original pulse train.

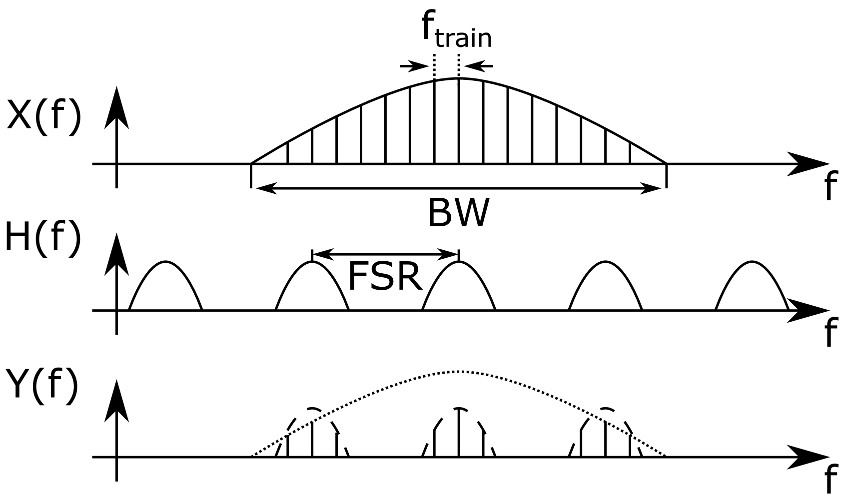

Figure 2.4: Direct burst formation in the Fourier-domain with a linear, time-invariant spectral filter with spectral periodicity FSR from a pulse train with low repetition rate f_{train} and bandwidth BW

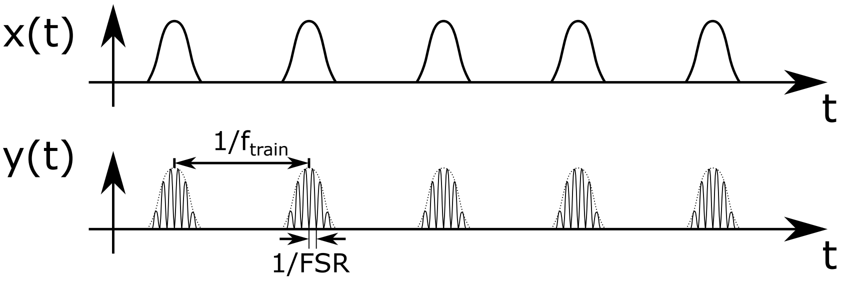

Figure 2.5: Direct burst formation in the time-domain with a linear, time-invariant spectral filter with spectral periodicity FSR from a pulse train with low repetition rate f_{train} and bandwidth BW

In the following, some examples of linear, time-invariant spectral filters for burst generation are presented:

Time-space-conversion

The combination of a grating and a lens, as it is shown in Fig. 2.6, was introduced by Froehly [7] and adopted by Weiner [8] in order to shape femtosecond optical pulses. It works like a physical Fourier-transformation, thus spectral components of an incoming plane wave are imaged on points of the Fourier-plane, which is the focal plane of the lens (Fig. 2.6). Therefore, it is possible to realize a spectral filter by placing a spatial amplitude- and/or phase-mask in the Fourier-plane. The use of a programmable spatial light modulator (SLM) as filter gives tunable control for the pulse shaping [9]. Especially in optical signal processing this approach is used, but in order to make the system compact the bulk gratings are replaced by an arrayed-waveguide grating (AWG) [10], whereas for high-energy bursts this setup is suitable.

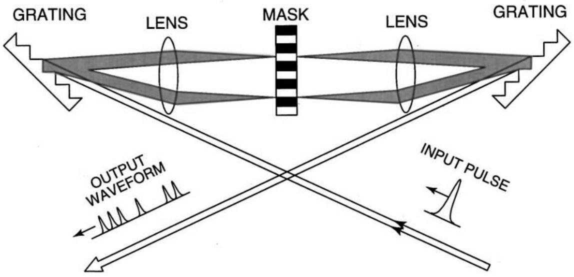

Figure 2.6: Femtosecond pulse shaping in the Fourier domain, Figure from [9]

The possibilities of shaping the bursts are manifold, as pointed out in [8] and generation of bursts with discretely tunable ps pulse spacing is possible when using a SLM as mask. However, drawbacks are spectral losses in the Fourier-plane when using amplitude filters and upper limits of a few picoseconds for the pulse spacing due to the finite resolution of filtering masks. By using a phase-only filter, the efficiency can be improved, though [11].

Arrayed Waveguide Grating (AWG)

Leaird et al. [12–14] demonstrated that by using an AWG with a FSR much smaller than the optical bandwidth, bursts are generated in every output channel of the AWG by each input pulse. The bursts from individual guides have a slight shift in output center wavelength. The intraburst repetition rate is given by the FSR, which is in this case

$$FSR = \Delta\tau^{-1} = \frac{c_0}{n_{eff}\Delta l}, \tag{2.4}$$

with $\Delta\tau$ being the delay increment per waveguide, c_0 the speed of light in vacuum, n_{eff} the effective refractive index of the waveguide and Δl the physical path length difference from guide to guide.

Fiber Bragg Grating

A spectral filter can also be realized in a fiber with a Fiber Bragg Grating (FBG). As a fiber approach, it represents a method with compactness, low coupling loss and low costs. The method is depicted in Fig. 2.7. Several FBG designs were reported, e.g. a chirped fiber grating [15] or superimposed FBGs [16]. Pulse bursts can be tailored with a wide variety by designing the spectral response of the FBG and it can be designed as a phase-only filter, which gives enhanced efficiency.

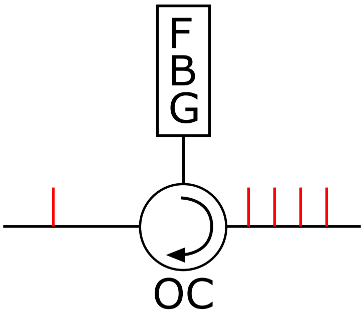

Figure 2.7: Generation of pulse bursts with a FBG: A single incoming pulse from the left enters the optical circulator (OC) and travels to the FBG, where it forms a burst, which is then sent to the output on the right side through the OC.

Coupled cavity

For the realization of phase-only filters coupled cavities were proposed by [17], which can be seen in Fig. 2.8. Design parameters of the filter are reflectivity r_i and round-trip phase ϕ_i of the cavities. As a phase-only filter, this method has the advantage of high efficiency.

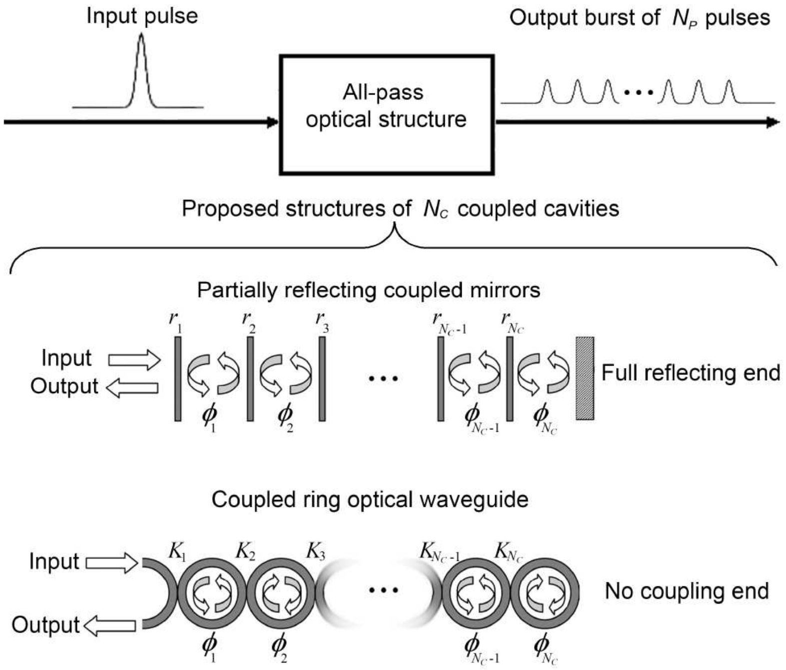

Figure 2.8: Phase-only coupled cavity filter for burst generation as proposed by [17], Figure from [17]

Birefringent crystals

By transmission of a single linearly polarized pulse through a birefringent crystal, the pulse can split into two pulses: one polarized along the ordinary axis and another polarized along the extraordinary axis of the crystal. Since those two components have, in general, a different group velocity in the crystal, they become separated temporally. Obviously, this approach is not restricted to a single crystal: By using n birefringent crystals rotated suitably, a pulse burst consisting of 2^n pulses is generated. In the end, pulses are recombined into a common polarization by a polarizer. An exemplary setup can be seen in Fig. 2.9.

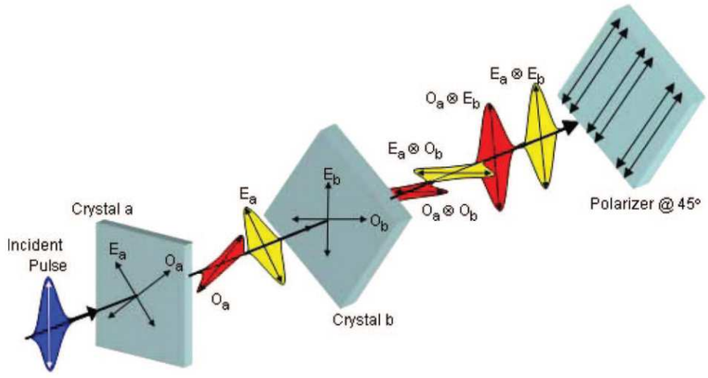

Figure 2.9: Generation of pulse bursts by using birefringent crystals, Figure from [18]

With this approach, bursts with ps-spaced pulses can be generated [18]. The number of pulses is restricted to 2^n, with n being the number of birefringent plates. The pulse spacing is set by the polarization-dependent group velocities in the crystal and hence by the thickness of the plates. Thus, the pulse spacing could be tuned by varying the incidence-angle of individual polarizations on the plates and ergo changing the relative optical path difference in the plates.

2.2.3 Nonlinear methods

Bursts can be formed with nonlinear methods, which utilize the nonlinear response of a medium to a fs pulse, which can be described by the nonlinear polarization P_n of order n in case of isotropic, homogeneous media as

$$P_n = \epsilon_0 \chi_n E_p^n, \tag{2.5}$$

where ϵ_0 is the dielectric constant and χ_n the electric susceptibility of order n and E_P the electric field of the pulse.

Induced modulational instability

As described in [22], an interplay between nonlinearities arising from the optical Kerr effect and anomalous dispersion leads to modulational instability (MI), which is a periodic modulation of amplitude and phase of a pulse. This periodic modulation can be utilized for pulse burst formation in a fiber, where the envelope of the burst is given by the envelope of the input pulse. In [19] it was shown, that by externally modulating an input pulse with a modulation wave, MI can be induced in order to tune the pulse spacing Δt in the burst generated according to the frequency detuning Δf of the input pulse carrier wave and the modulation wave as

$$\Delta t = \frac{1}{\Delta f.} \tag{2.6}$$

The number of pulses N is limited by the input pulse duration τ_p by

$$N = \frac{\tau_p}{\Delta t}. \tag{2.7}$$

This method can only be realized in the anomalous dispersion regime, which restricts the successible frequency range and individual pulse parameters in the burst cannot be controlled.

2.2.4 Vernier effect

The concept of using the Vernier effect is to combine the cavity of an oscillator with another cavity, whose round-trip time is slightly detuned from the oscillator cavity (Fig. 2.10). For this concept, pulse accumulation needs to be introduced, during which the cavity is open to the incoupling of new pulses, while sustaining the pulse energy of the pulses that are already inside. If this is the case, a burst can be formed and the temporal pulse spacing Δt is related to the cavity detuning ΔL, which is the difference of oscillator length L_{OSC} and cavity length L_{CAVITY}, by

$$\Delta t = \frac{2|\Delta L|}{c_0} = \frac{2|L_{OSC} - L_{CAVITY}|}{c_0}, \tag{2.8}$$

where c_0 is the speed of light in vacuum. This corresponds to an intraburst repetition rate f_{burst} of

$$f_{burst} = \frac{1}{\Delta t} = \frac{c_0}{2|L_{OSC} - L_{CAVITY}|}. \tag{2.9}$$

Eqs. 2.8,2.9, hold for linear cavities, while for ring cavities the factor 2 is omitted. Both, passive and amplifier cavities can be used.

With the Vernier effect, a practically arbitrary short and continuously-tunable pulse spacing Δt can be achieved by adjusting the cavity detuning ΔL by moving one of the mirrors in the cavity, e.g. $M3$ in Fig. 2.11d. A pulse spacing of $1ps$ would need a cavity detuning of $150\mu m$, which can be easily set with a micrometer screw. However, a pulse spacing in the ps-regime will lead to different problems when amplifying bursts, which can prevent efficient amplification of bursts with ps pulse spacing (Sec. 3.4). The number of pulses N can be scaled easily by adjusting the accumulation time window, but for a given pulse spacing Δt it is restricted to

$$N < \frac{2L_{CAVITY}}{c_0 \Delta t}, \tag{2.10}$$

with c_0 being the speed of light in vacumm, because otherwise individual parts of the burst would start to overlap while circulating in the cavity. Therefore, it wouldn't be possible to extract the pulses out of the cavity in an ordered way. However, for a cavity with $L_{CAVITY} = 3m$ and a burst with $\Delta t = 1ps$, the maximum number of pulses would be 20000, which shows the high scalability. An important advantage of this method is, because the repetition rate of the oscillator pulse train is much lower than the resulting intraburst repetition rate, that it is possible to control individual pulse parameters, like peak intensity and intraburst CEP, before the pulses reach the cavity. Thus, the tuning of individual pulse parameters in the burst can be achieved (Sec. 3).

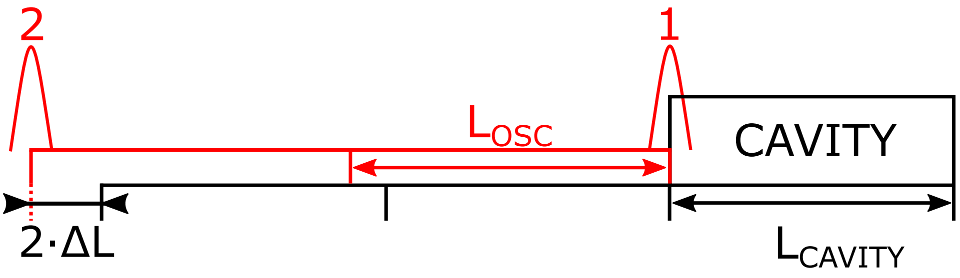

Figure 2.10: Concept of using the Vernier effect for burst generation

Vernier effect with a regenerative amplifier and a Pockels-cell

In order to realize the Vernier effect, a regenerative amplifier (RA) can be used as cavity, where the cavity lengths L_{OSC}, L_{RA} are slightly detuned, such that consecutive pulses become separate by a time Δt according to Equ. 2.8 with $L_{CAV} = L_{RA}$. As pulse accumulation mechanism a voltage protocol for a Pockels cell (PC) used as electro-optic switch for the RA [20] can be applied. When the PC voltage V_{PC} is zero, pulses will only fulfill one round-trip in the RA and leave it afterwards (Fig. 2.11a). Pulses can be accumulated in the RA, if V_{PC} is set to an intermediate voltage level, making the RA partly transparent (Fig. 2.11b). Losses at the thin-film polarizer (TFP2) can be compensated by the round-trip gain. Setting V_{PC} to full voltage V_{full} closes the RA cavity, leading to amplification of the burst (Fig. 2.11c). Afterwards, the burst can be released by setting V_{PC} back to zero (Fig. 2.11d). Additionally, optical isolation is depicted in Fig. 2.11, consisting of a Faraday rotator (FR), a thin-film polarizer (TFP1) and a polarizer (P) in order to avoid backreflections to the oscillator and to separate incoming and outgoing pulses. A $\lambda/2$ waveplate is also depicted, which is for tuning the polarization of the incoming pulses properly.

One limitation, that is given by combining the Vernier effect with a RA like this, is the upper limit of burst repetition rate f_{rep}, which is given by

$$f_{rep} \leq \frac{1}{t_{rise} + n \cdot t_{round-trip,RA} + t_{fall}}, \tag{2.11}$$

with t_{rise}, t_{fall} being the rise- and fall-time of the PC, n the number of round-trips and $t_{round-trip,RA}$ the round-trip time in the RA. This limit is usually set to be $1kHz$ up to a few hundreds of kHz by tuning the number of round-trips n, together with the trade-off of lower amplified burst energy the higher the burst repetition rate, because of the lower number of round-trips and hence, a lower total gain.

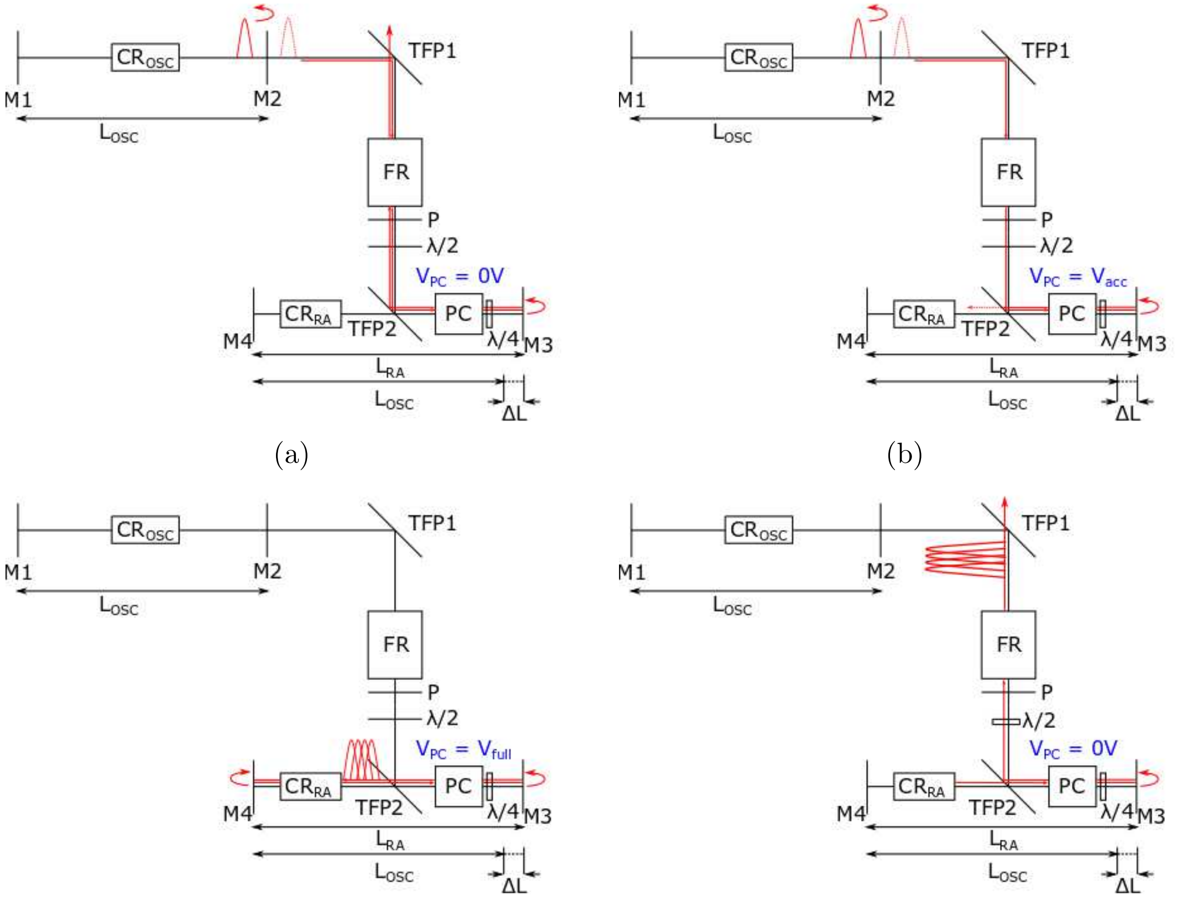

(a) (b) (c) (d)

Figure 2.11: Burst generation by utilizing the Vernier effect with a regenerative amplifier (RA), a Pockels-cell (PC) and a protocol for the Pockels cell voltage V_{PC} a) $V_{PC} = 0V$: incoming pulses from the oscillator leave the RA after one round-trip and travel to the output at TFP1. b) $V_{PC} = V_{acc}$: burst formation, pulses are accumulated in the RA. c) $V_{PC} = V_{full}$: amplification of the burst at full Pockels cell voltage d) $V_{PC} = 0V$: the amplified pulse burst is released to the output at TFP1. CR_{OSC}, CR_{RA}...crystal of oscillator and regenerative amplifier; M1...M4...mirrors; TFP1,TFP2...Thin Film Polarizers; FR...Faraday Rotator; PC...Pockels cell; L_{OSC}, L_{RA}...length of OSC, RA

2.3 Comparison of recent methods

Tab. 2.2 shows a comparison of recent burst generation methods with respect to relevant burst parameters. The potential of the Vernier effect can be seen, combining wide and continuous tunability of the pulse spacing (lower limit in the sub-ps range), a high scalability of the number of pulses and control over individual pulse parameters, like peak intensity $I_{peak,i}$ and intraburst CEP ϕ_{i1}, which makes it very attractable for a number of applications (Chapter 4). There is an upper limit for the burst repetition rate f_{rep} in case of using a RA as cavity, which is given by Equ. 2.11, although hundreds of kHz can be achieved with the drawback of lower output burst energy. However, amplification of the burst from oscillator energies (typically several nanojoules) to millijoules is given by this method, even for ps-spaced pulse bursts as it is shown in Sec. 3.4.2 by suppressing the formation of spectral modes. The RA also allows the capability of stabilizing intraburst CEP drifts, as it is shown in Sec. 3.5, which can prevent the necessity of stabilizing the CEP of the source oscillator pulse train and allows the generation of reproducible fs pulse bursts.

	pulse picker	spectral filters	nonlinear	Vernier
f_{rep}	MHz	MHz	MHz	MHz (kHz with RA)
Δt	$\geqslant$ ns	few ps $\geqslant$	$\geqslant$ sub-ps	$\geqslant$ sub-ps
Δt tunability	discrete	discrete	continuous	continuous
N	high	intermediate	high	high
$I_{peak,i}$ tunability	individually	partly	none	individually
$\Delta\phi_{i1}$ tunability	individually	partly	none	individually

Table 2.2: Comparison of recent burst generation methods

3 Generation and amplification of femtosecond Vernier bursts with controlled and stabilized intraburst CEPs

On the foundation of utilizing the Vernier effect, control and stabilization of intraburst CEPs is realized, which strongly enhances the capabilities of burst generation and amplification. After a short introduction into Chirped Pulse Amplification (Sec. 3.1), the concept of the new generation method for bursts (Sec. 3.2) and the setup realized in the laboratory is presented (Sec. 3.3). This method allows efficient amplification of fs pulse bursts with a sub-ps pulse spacing up to millijoule energies by intraburst CEP scrambling (Sec. 3.4). For realizing stable, reproducible bursts, intraburst CEP stabilization is presented (Sec. 3.5), which leads to cancellation of the intraburst CEP drift and thus, phase-locked pulses in the burst.

3.1 Chirped Pulse Amplification (CPA)

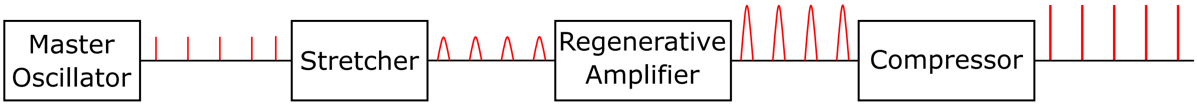

Figure 3.1: Concept of Chirped Pulse Amplification

When amplifying fs pulses, it has to be taken care of high peak intensities, that can already develop at low pulse energies for such short pulses in the amplifier. Otherwise, they can lead to severe optical damage in the amplifier. As demonstrated by Strickland and Mourou [23] (Nobel Prize in Physics 2018), this can be avoided by stretching the pulse temporally before amplification and by compressing it afterwards (Fig. 3.1). Usually, compressing and stretching is done by using gratings, prisms or a combination of both, which disperse the pulses. This imprints a strong chirp, i.e. rising or falling frequency over time, on the pulses.

3.2 Concept

The concept can be seen in Fig. 3.2: Starting from the burst generation method utilizing the Vernier effect, as depicted in Fig. 2.11, a stretcher, a compressor and an acousto-optical modulator (AOM) is implemented into the setup. The AOM splits the original beam into two beams: a diffracted and a non-diffracted one. The former is used as high-repetition rate reference beam and the latter is used as seed for the pulse burst. Both enter the regenerative amplifier (RA). However, the reference beam only fulfills a single round-trip, exiting the RA afterwards and being directed to a spectrometer (SPEC). There it interferes spectrally with a copy of the next coming reference pulse, which is reflected at the beam splitter (BS). This spectral interference gives information about drifts of the cavity detuning ΔL and therefore also the relative phases of the pulses in the burst, i.e. the intraburst CEPs ϕ_{i1}, as will be explained in further detail in Sec. 3.5.

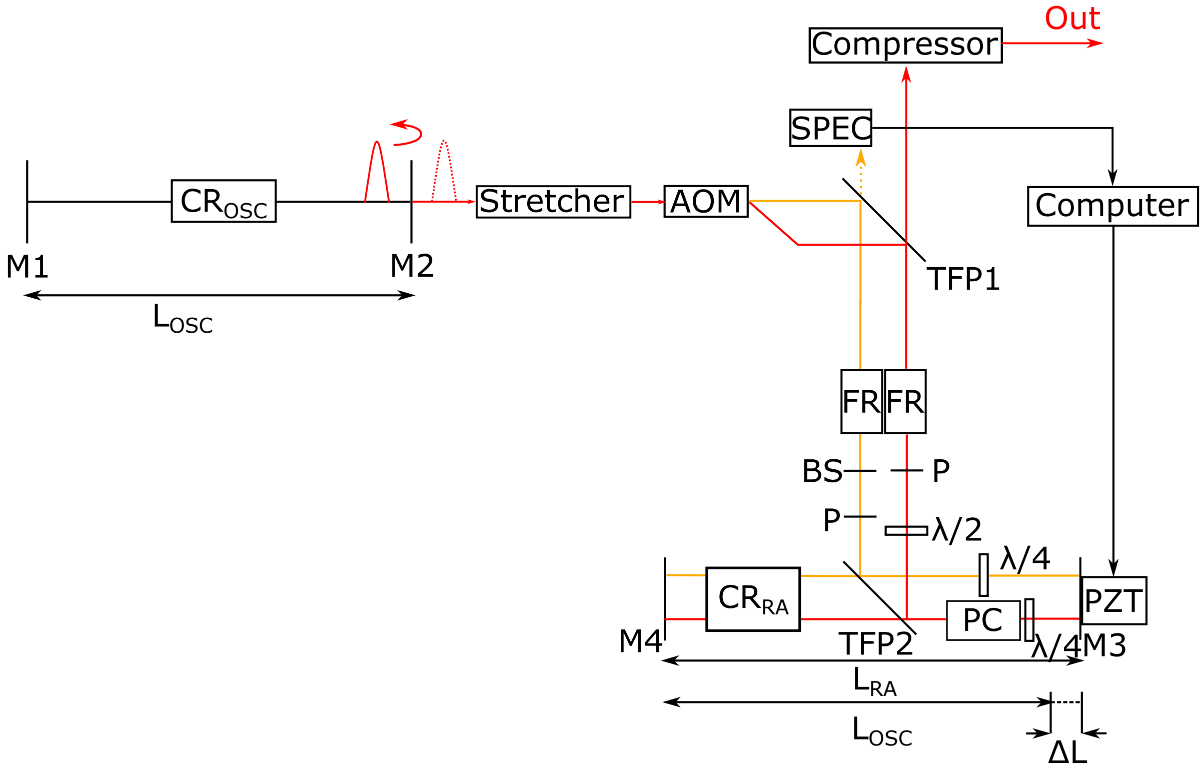

Figure 3.2: Concept of the pulse burst generation method utilizing the Vernier effect, CPA, an AOM and measurement of intraburst CEP drifts

Overall, the changes compared to the setup depicted in Fig. 2.11 lead to additional capabilities:

- The AOM can set the individual peak intensities and intraburst CEPs of the burst.
- CPA in combination with the AOM allows amplification of the bursts to millijoule energies (See Sec. 3.4).

- By measuring the spectral interference of the reference beam, intraburst CEP drifts can be measured and controlled by driving a piezoeletric transducer (PZT), which sets the cavity detuning ΔL (See Sec. 3.5).

3.3 Realization in the laboratory

The realization of the proposed method in the laboratory can be seen in Figs. 3.3-3.6. The pulses generated with a master oscillator (FLINT, Light Conversion; Yb:KGW, $f_{rep} = 75$MHz, $2.5W$ output power, $200fs$ pulse duration) first enter a stretcher, where they are stretched to several hundreds of picoseconds (Fig. 3.3). The input port of the stretcher in Fig. 3.3 also serves as output port. Additionally, optical isolation was implemented with a Faraday isolator, consisting of a thin-film polarizer (TFP), a $\lambda/2$ waveplate and a Faraday rotator (FR), in order to prevent pulses being reflected back into the master oscillator.

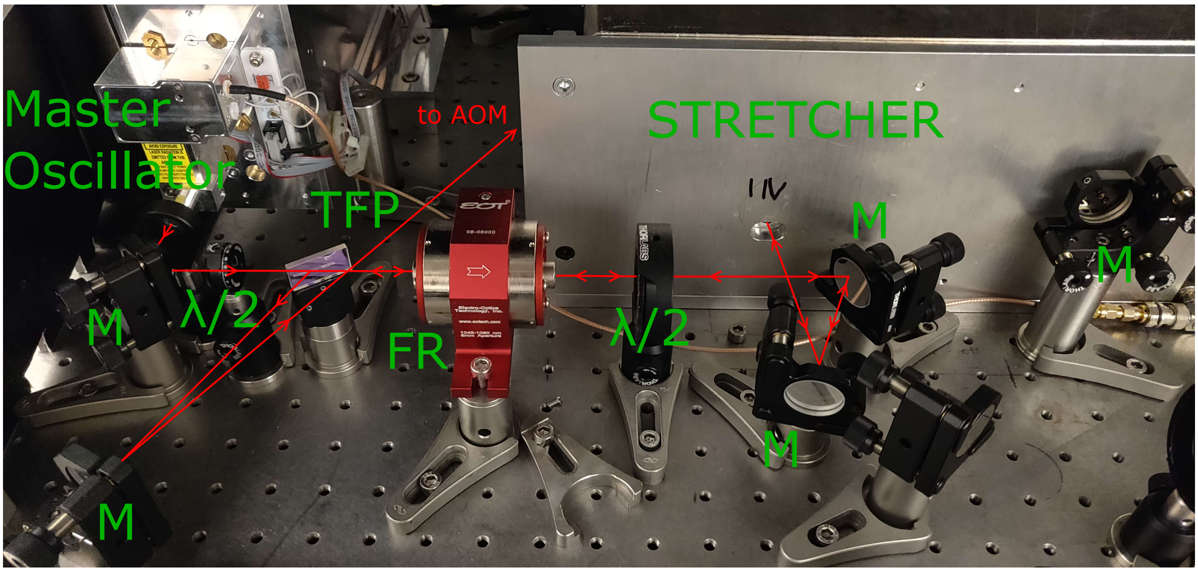

Figure 3.3: Setup in the lab from master oscillator through the stretcher to the entrance of the AOM

Thereupon, the pulse beam is split into two beams by the AOM (Fig.3.3b): the non-diffracted reference beam (orange) and the diffracted seed beam (red). Therefore, the AOM works as pulse picker for the seed pulses. The AOM is synchronized electronically with the trigger-signal from the oscillator. A lens is placed after the AOM to recollimate the beams.

By using a prism-combination, the seed beam is separated further from the reference beam making separate adjustments feasible (Fig. 3.3c).

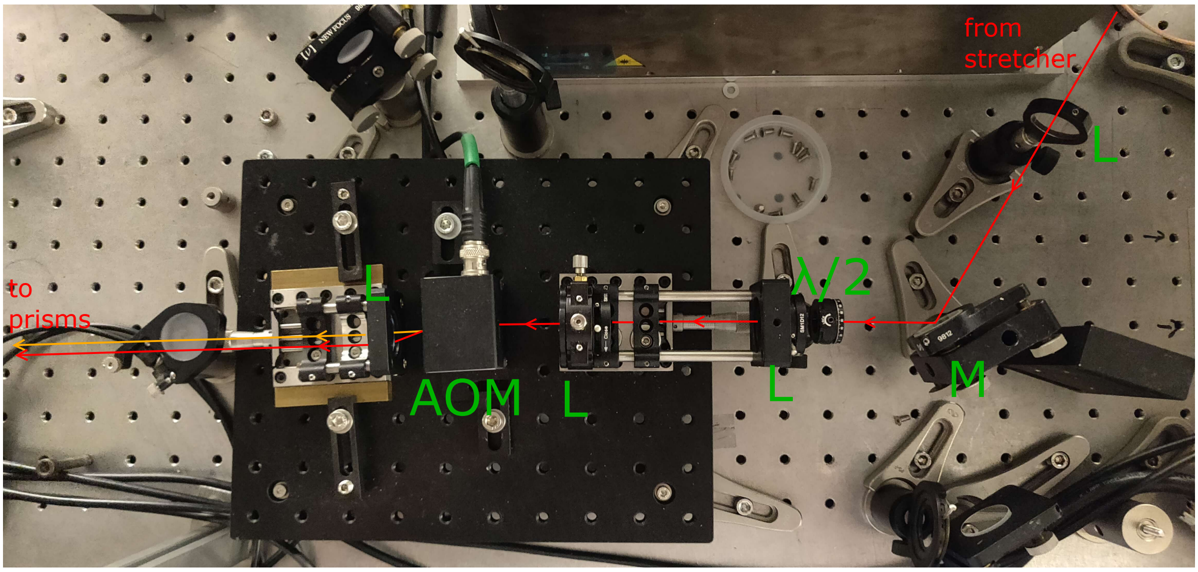

Figure 3.4: Setup in the lab through the AOM

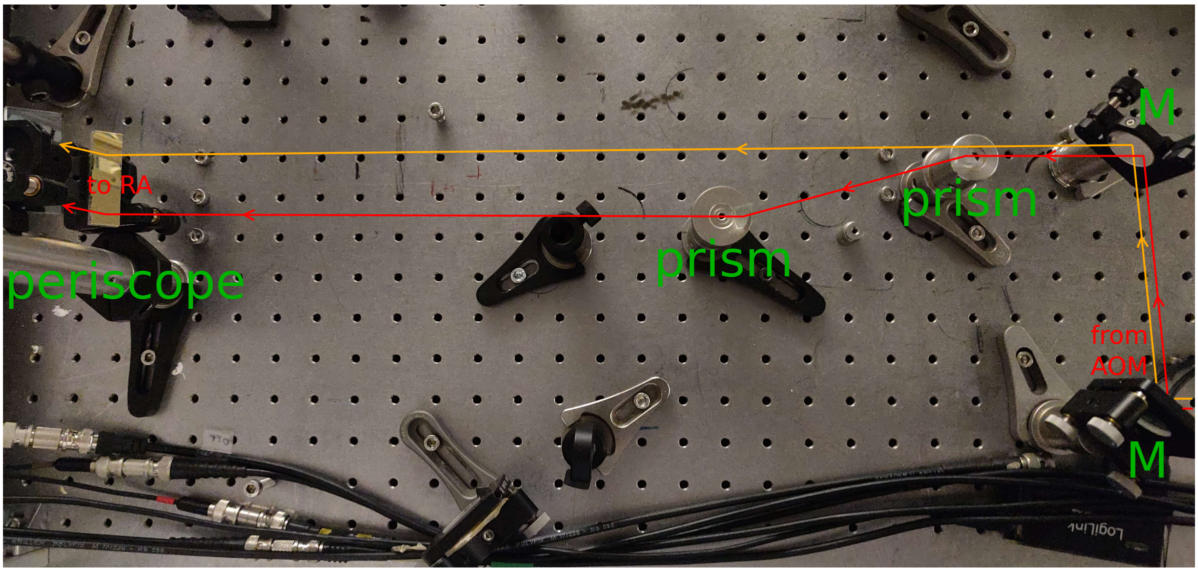

Figure 3.5: Setup in the lab through double prism to the entrance of the RA

Then, they are directed into an Yb:CaF2 RA, where adjustments are done in such a way, that both beams can be incoupled sequentially with two mirrors each (MR1, MR2 for the reference beam; MS1, MS2 for the seed beam), with the reference beam being incoupled first. They both enter the RA cavity through a double thin-film polarizer (DTFP) consisting of two exactly parallel TFPs. Generally it is important, that reference and seed beam both share as many optical components as possible in order to assure the quality of the reference, which could be spoiled by influences like mechanical or thermal noise introduced by separate components. Also here it was taken care, that no reflections back to the master oscillator can happen by implementing Faraday isolators (TFP, FR, $\lambda/2$ waveplate). Additionally, this configuration allows to separate the incoming from the outgoing beam. The end mirror (EM1) is a flat mirror mounted on a translation stage (TS), which can be tuned manually with a micrometer screw and finer with a piezomotor. The other end mirror (EM2) is a curved mirror responsible for focusing in the cavity in order to achieve a bound cavity mode and get an efficient round-trip gain. The cavity detuning ΔL can be set by applying a voltage on a piezoelectric transducer (PZT) with a mirror mounted on. Other things, which can be seen in Fig. 3.6 are: the Pockels cell (PC) and its driver, the pump laser diode (LD; nLight, Pearl P16, continuous-wave, wavelength-stabilized, $976nm$ center wavelength) together with its optics (framed blue), the water-cooled crystal (CR) and a water-cooled beam dump (BD) for the pump laser. It is very important for the interferometric stabilization of the cavity detuning drift (Sec. 3.5), that the heat introduced by the pump is properly directed out of the cavity by the beam dump BD, since the phase stabilization is sensitive to temperature changes of mK.

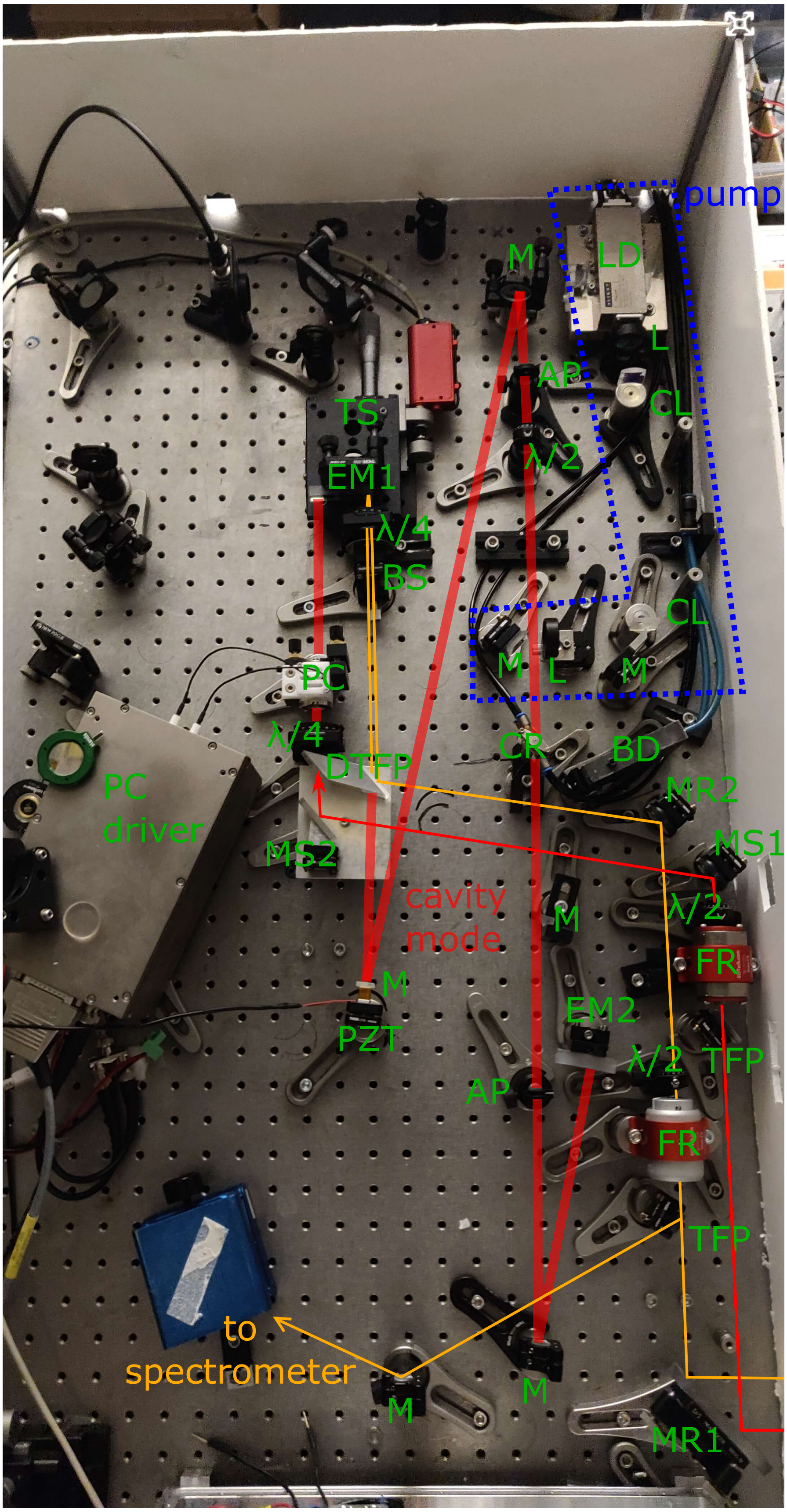

Figure 3.6: Setup of the RA in the laboratory

3.4 Efficient amplification of fs pulse bursts with ps pulse spacing

In this section, first the spectral characteristics of a pulse burst showing the formation of spectral modes is presented (Sec. 3.4.1). These spectral modes can lead to limitations regarding the amplification of fs pulse bursts. Therefore, phase scrambling is demonstrated in Sec. 3.4.2.

3.4.1 Spectral mode formation

When a pulse $E(t)$ is delayed by some time Δt, it is modulated in the frequency-domain $E(\omega)$ as

$$E'(\omega) = E(\omega) \cdot e^{-j\omega\Delta t}. \tag{3.1}$$

A pulse burst consisting of N equal pulses, which are delayed to each other by time Δt and show a constant intraburst CEP shift $\Delta\phi_{CEP}$, can be described as

$$E(t) = \sum_{n=0}^{N-1} E_P(t - n\Delta t) e^{jn\Delta\phi_{CEP}}, \tag{3.2}$$

with $E_P(t)$ being the waveform of a single pulse. The intraburst CEP shift $\Delta\phi_{CEP}$ is assumed to be constant over the burst duration, since it is expected to drift on a much longer time scale (Sec. 3.5.3). The Fourier-transform of Equ. 3.2 is

$$\begin{aligned}
E(\omega) &= \sum_{n=0}^{N-1} E_P(\omega) e^{-jn\Delta t\omega} e^{jn\Delta\phi_{CEP}} && (3.3)\\
&= E_P(\omega) \sum_{n=0}^{N-1} e^{-jn(\Delta t\omega - \Delta\phi_{CEP})} && (3.4)\\
&= E_P(\omega) \cdot \frac{1 - e^{-jN(\Delta t\omega - \Delta\phi_{CEP})}}{1 - e^{-j(\Delta t\omega - \Delta\phi_{CEP})}}, && (3.5)
\end{aligned}$$

which gives after some calculation

$$\begin{aligned}
E(\omega) &= E_P(\omega) \cdot f(\omega; \Delta t, N, \Delta\phi_{CEP}) && (3.6)\\
f(\omega; \Delta t, N, \Delta\phi_{CEP}) &= -\frac{\sin\left(\frac{N(\Delta t\omega - \Delta\phi_{CEP})}{2}\right)}{\sin\left(\frac{\Delta t\omega - \Delta\phi_{CEP}}{2}\right)} e^{-j\frac{N-1}{2}(\Delta t\omega - \Delta\phi_{CEP})} && (3.7)
\end{aligned}$$

The single pulse spectrum $E_P(\omega)$ is the envelope of the burst spectrum, while $f(\omega; \Delta t, N, \Delta\phi_{CEP})$ describes the formation of spectral modes, which become narrower and more intense the higher the number of pulses N in the burst (Fig. 3.7) and the shorter the pulse spacing Δt. More precisely, the zero-to-zero width $\Delta\Omega_{zz}$ of each maximum is

$$\Delta\Omega_{zz} = \frac{4\pi}{N\Delta t} = \frac{4\pi}{T_{burst}}, \tag{3.8}$$

with $T_{burst} = N\Delta t$ being the duration of the burst. The period $\Delta\Omega$ of spectral modes in the frequency-domain depends only on the pulse spacing Δt or rather the intraburst repetition rate f_{burst} (Fig. 3.8)

$$\Delta\Omega = \frac{2\pi}{\Delta t} = 2\pi f_{burst}, \tag{3.9}$$

whereas the offset on the frequency axis depends on the intraburst CEP shift $\Delta\phi_{CEP}$ (Fig. 3.9) and the pulse spacing Δt for $\Delta\phi_{CEP} \neq 0$

$$\Omega_{offset} = \frac{\Delta\phi_{CEP}}{\Delta t}. \tag{3.10}$$

It should be noted, that this is the spectrum of a single burst. This formulation can be extended to an infinite train of bursts, which can be seen in Sec. 3.5.4.

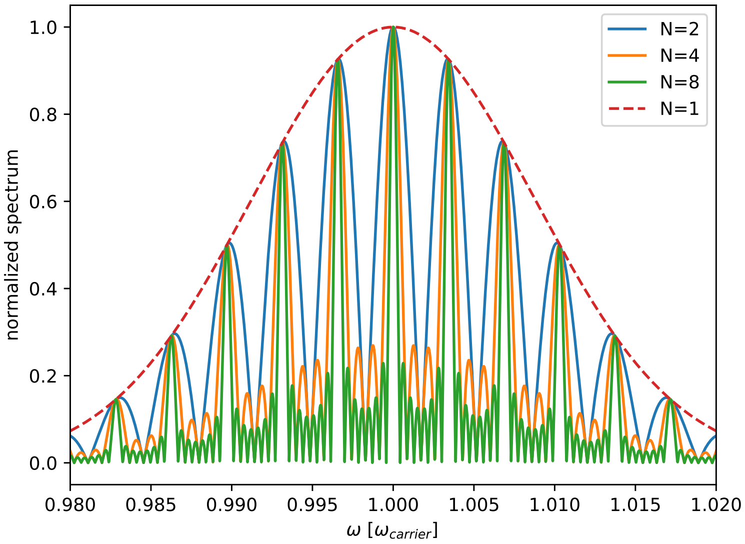

Figure 3.7: Formation of spectral modes, according to Eqs. 3.6 and 3.7, depending on the number of pulses N in the burst with a pulse spacing Δt of $1ps$ and $\Delta\phi_{CEP} = 0$

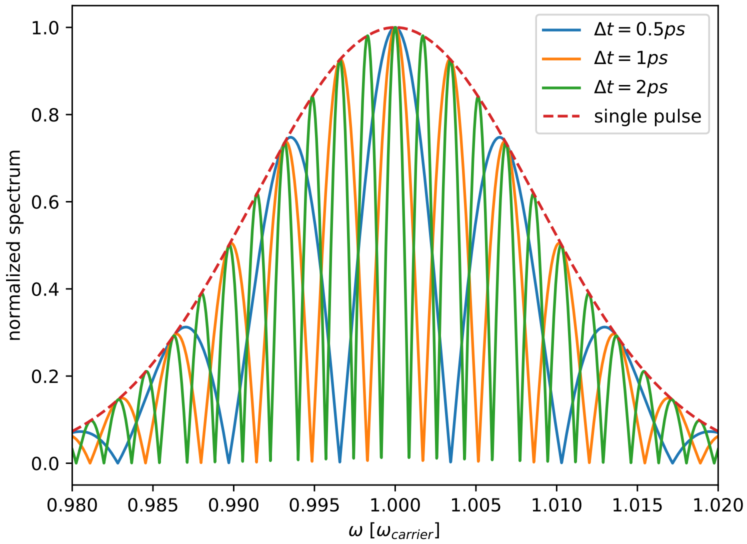

Figure 3.8: Formation of spectral modes, according to Eqs. 3.6 and 3.7, depending on the pulse spacing Δt for $N = 2$ pulses in the burst and $\Delta\phi_{CEP} = 0$

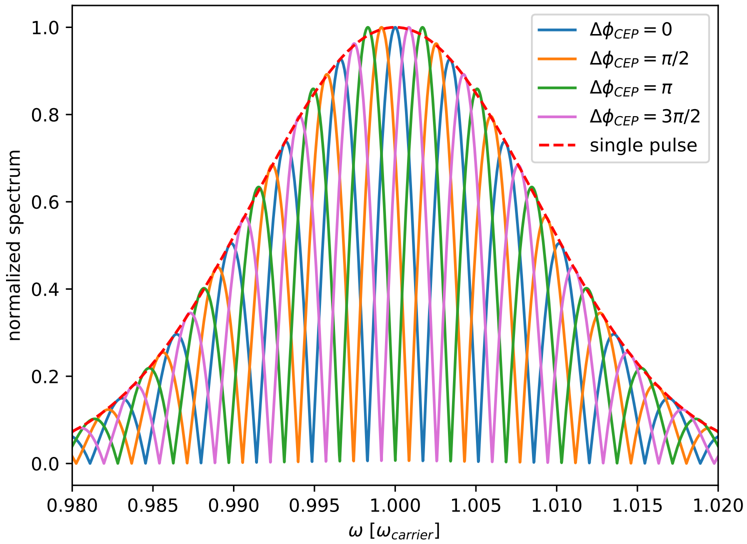

Figure 3.9: Formation of spectral modes, according to Eqs. 3.6 and 3.7, depending on the intraburst CEP shift $\Delta\phi_{CEP}$ for $N = 2$ pulses in the burst and a pulse spacing Δt of $1ps$

3.4.2 Phase scrambling

When amplifying pulse bursts with ps pulse spacing with CPA, where each pulse is stretched to several hundreds of picoseconds, the pulses in the burst almost overlap completely. Because of this overlap and the strong chirp impressed on the pulses during CPA, the spectrum translates directly from the frequency-domain to the time-domain. Thus, strong intensity-peaks are formed in the time-domain during amplification, which can lead to optical damage in the amplifier. Considering a maximum single pulse energy $E_{p,max}$ acceptable in the amplifier, the maximum acceptable burst energy $E_{burst,max}$ will be

$$E_{burst,max} = N \cdot E'_{p,max} = N \cdot \frac{E_{p,max}}{N^2} = \frac{E_{p,max}}{N} \tag{3.11}$$

where $E'_{p,max}$ gives the maximum acceptable single pulse energy in the burst in case of constructive spectral interference and N being the number of pulses in the burst. Therefore, the accessible energy range is strongly reduced.

The formation of strong spectral modes can be avoided by suppressing the constructive interference. This can be done by manipulating the phases of the individual pulses in such a way, that destructive interference is favoured. For a higher number of pulses this means, that the phases are evenly distributed, which is called phase-scrambling (Fig. 3.10). In our setup, this tuning of the intraburst CEPs can be done with the AOM and allowed us to successfully test the phase scramble approach (Fig. 3.11).

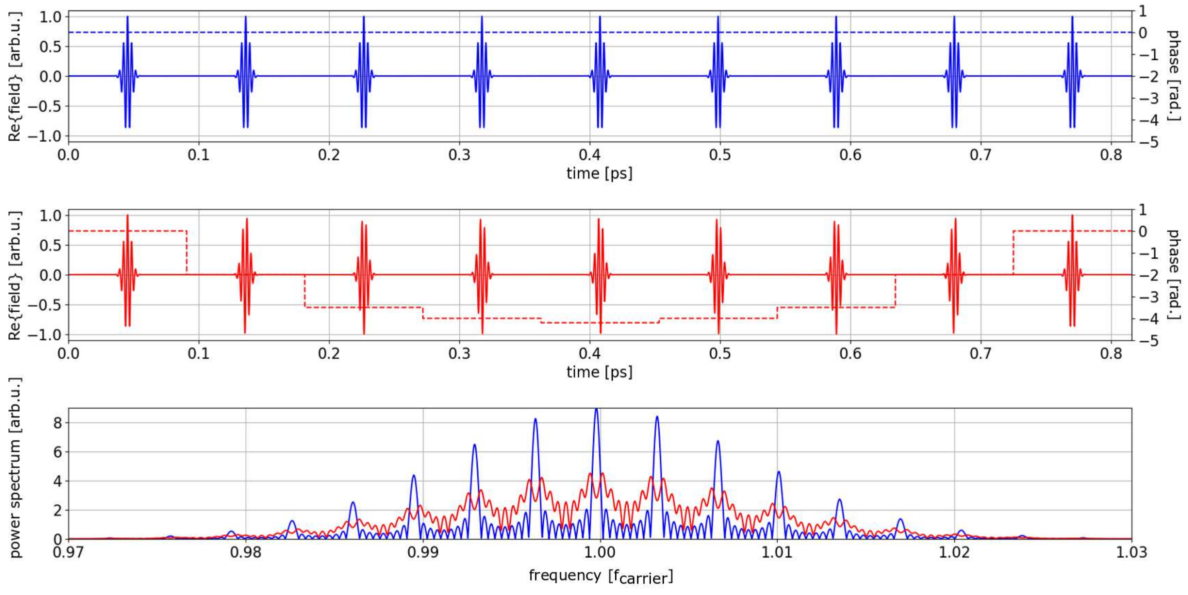

Figure 3.10: Numerically simulated formation of spectral modes depending on the intraburst CEPs. A burst in the time-domain with (Top) Unscrambled intraburst CEPs (Middle) Scrambled intraburst CEPs (Bottom) Spectra for (blue) unscrambled and (red) scrambled intraburst CEPs

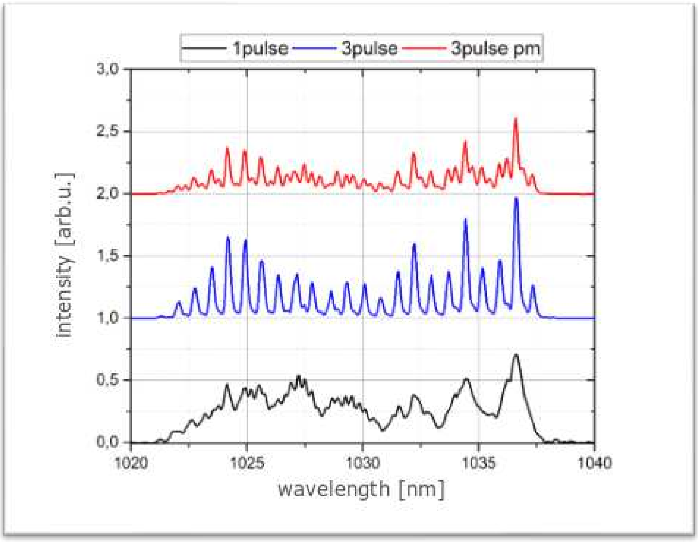

Figure 3.11: Measured spectra of pulse bursts with 3 pulses and a pulse spacing of $4.8ps$ depending on the intraburst CEPs: (Top) Scrambled CEPs (Middle) Unscrambled CEPs (Bottom) Single pulse spectrum

3.5 Intraburst CEP stabilization

This section begins with explaining the operating principle of the intraburst CEP stabilization (Sec. 3.5.1), which includes a conceptual description, an explanation of the intraburst CEP drift measurement and the PID control. Then, the program developed for experimental control and data acquisition is presented (Sec. 3.5.2). Afterwards results of the intraburst CEP stabilization are shown and discussed (Sec. 3.5.3).

3.5.1 Operating principle

As seen in the previous sections, the spectrum of the pulse burst depends strongly on the intraburst CEPs. Thus, in order to generate reproducible pulse bursts these phases need to be stable over time. The intraburst CEPs can be formulated as a function of the lengths L_{MO} and L_{RA} of master oscillator (MO) and regenerative amplifier (RA), respectively. However, these change over time mainly due to thermal drifts and mechanical vibrations:

$$L_{MO}(t) = L_{MO,0} + \delta L_{MO}(t) \tag{3.12}$$

$$L_{RA}(t) = L_{RA,0} + \delta L_{RA}(t) \tag{3.13}$$

where $L_{MO,0}$, $L_{RA,0}$ are reference lengths of MO and RA at some fixed time, respectively and $\delta L_{MO}(t)$, $\delta L_{RA}(t)$ are the time-dependent drifts. The cavity detuning ΔL will then be

$$\Delta L(t) = L_{MO}(t) - L_{RA}(t) = \Delta L_0 + \delta L(t) \tag{3.14}$$
$$\delta L(t) = \delta L_{MO}(t) - \delta L_{RA}(t) \tag{3.15}$$

with $\delta L(t)$ being the time-dependent drift of the cavity detuning, which is directly related to the intraburst CEP shift $\Delta\phi_{CEP}$ and its drift $\delta\phi_{CEP}$

$$\Delta\phi_{CEP} = k_0 2\Delta L_0 \tag{3.16}$$
$$\delta\phi_{CEP}(t) = k_0 2\delta L(t), \tag{3.17}$$

where again the factor 2 can be omitted for ring cavities and k_0 being the carrier wavenumber. The intraburst CEP drift $\delta\phi_{CEP}(t)$ can be measured and used as a control quantity for a piezoelectric transducer (PZT). With a mirror attached to the PZT, the RA length can be varied such that

$$\delta L_{RA}(t) = \delta L_{MO}(t) \tag{3.18}$$

leading to a temporally stable cavity detuning ΔL and thus, cancelling the intraburst CEP drift $\delta\phi_{CEP}(t)$ (Fig. 3.12). Bursts can then be called phase-locked, since they can be generated with reproducible phases.

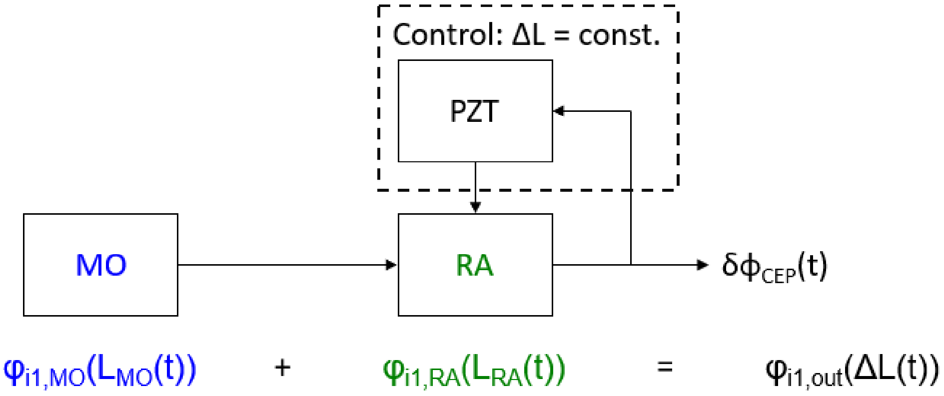

Figure 3.12: Depiction of the intraburst CEP stabilization concept

Measurement of the intraburst CEP drift

The measurement of the intraburst CEP drift $\delta\phi_{CEP}(t)$ is done by spectrally interfering two consecutive pulses from the reference beam: one that fulfilled a full round-trip in the RA cavity and one that was directly reflected from the entrance of the RA (Sec. 3.3).

The interference spectrum can be seen on the left in Fig. 3.13[1], which shows periodic modulations with period Δf_{mod}, which is given by

$$\Delta f_{mod} = \frac{c_0}{2(L_{OSC} - L_{BS,RA} - L_{RA})} \tag{3.19}$$

with c_0 being the speed of light in vacuum, L_{OSC} and L_{RA} the length of oscillator and RA and $L_{BS,RA}$ the distance from beamsplitter (BS) to RA. The latter can be set such that the modulation can be well resolved on the spectrometer. By Fourier-transforming the interference spectrum, the interference modulation can be seen as local maximum (Fig. 3.13 middle). Hence, the phase of the modulation $\phi(t)$ can be evaluated at this point t_0. Since this phase evolves from interference of a reference pulse with its successor, it is equal to

$$\begin{aligned} \phi(t) &= 2k_0(L_{OSC}(t) - L_{BS,RA}(t) - L_{RA}(t)) && (3.20)\\ &= 2k_0(\Delta L(t) - L_{BS,RA}(t)) && (3.21)\\ &= 2k_0(\Delta L_0 - L_{BS,RA,0} + \delta L(t) - \delta L_{BS,RA}(t)) && (3.22)\\ &\approx \phi_0 + \delta\phi_{CEP}(t), && (3.23) \end{aligned}$$

with the approximation $\delta L_{BS,RA}(t) \ll \delta L(t)$, since the cavity detuning of oscillator and RA involves much more components, which are susceptible to drift. Therefore, the drift of this phase is equal to the intraburst CEP drift $\delta\phi_{CEP}(t)$.

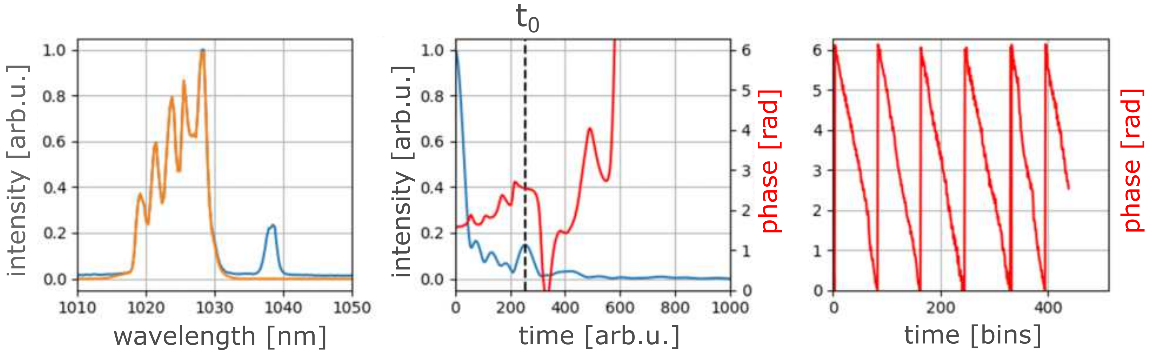

Figure 3.13: Measurement of the cavity detuning drift: (Left) Spectrum from the reference beam spectrometer (Middle) Fourier-transform of the spectrum, showing the spectral interference peak at t_0 (Right) Phase of the spectral interference over time

---

[1] Also a strong suppression of the spectrum above 1030nm can be seen, which is due to gain compensation. The spectral intensity is decreased in this range by inserting screws in the Fourier-plane of the stretcher in order to avoid gain narrowing in the amplifier.

PID control

A PID controller was implemented in software, which calculates the voltage v_i from the phase $\phi(t_i)$ at time bin i and forwards it to the PZT :

$$v_i = v_{p,i} + v_{I,i} + v_{D,i} \tag{3.24}$$

$$v_{p,i} = \gamma k e_i \tag{3.25}$$

$$v_{d,i} = -\gamma k_d \frac{v_i - v_{i-1}}{dT} \tag{3.26}$$

$$v_{I,i} = v_{I,i-1} + \gamma k_i dT e_i \tag{3.27}$$

$$e_i = \phi_i - \phi_0 \tag{3.28}$$

with k, k_i, k_d being the control parameters, dT set roughly to the (with Python achievable) framerate of the spectrometer ($\approx 5ms$), $\gamma = \pm 1$ as sign for the control and ϕ_0 the reference phase, that can be set at any time.

3.5.2 Program

For realizing the intraburst CEP stabilization, a software for data acquisition and experimental control was written, which was done in Python.

Functional overview and GUI

The functional diagram of the program can be seen in Fig. 3.14. Parameters for the control are read from a file, when starting the program. Then, constantly during operation, the spectra from the spectrometers for the reference beam and (optionally) for the amplified pulse burst are read, the voltage needed for maintaining control of the detuning is calculated and sent to the PZT, the data (wavelength range, delays, spectra, voltages) is written to a file and displayed in the GUI, which can be seen in Fig. 3.15. The program gives the user the opportunity to set at any time the control parameters k, k_i, k_d, the evaluation point t_0 for $\phi(t)$ (called "ref. point" in the program) and the reference phase ϕ_0, where the current phase is saved as reference.

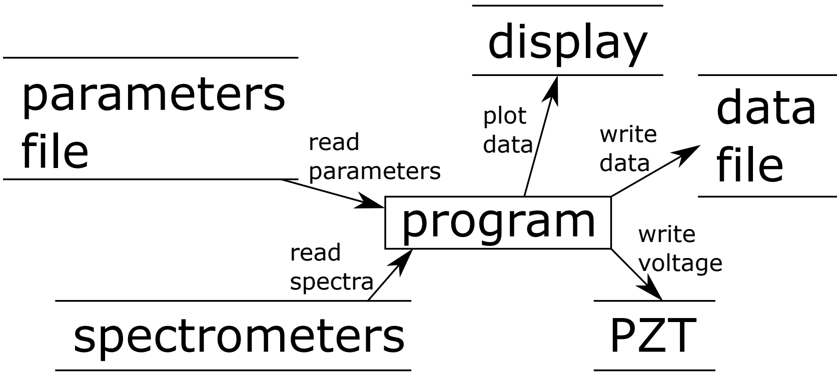

Figure 3.14: Functional diagram of the program

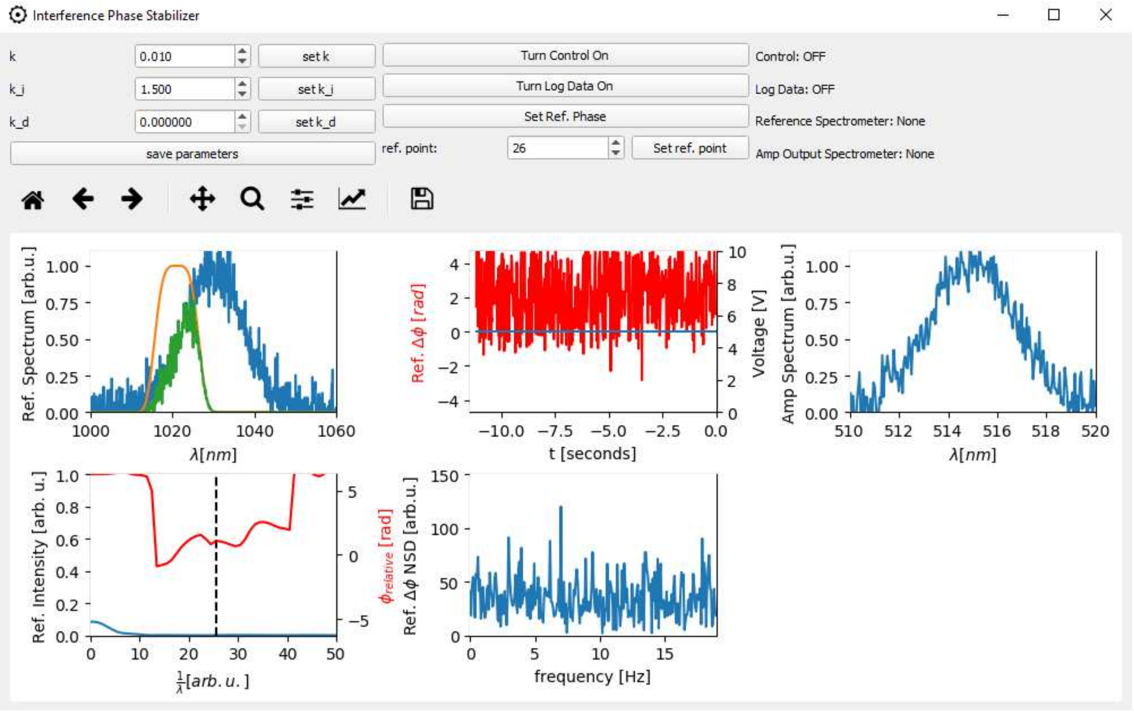

Interference Phase Stabilizer

k 0.010

k_i 1.500

k_d 0.000000

ref. point: 26

Control: OFF

Log Data: OFF

Reference Spectrometer: None

Amp Output Spectrometer: None

Figure 3.15: GUI of the program

3.5.3 Results

The software, developed in the course of this thesis (Sec. 3.5.2), was tested by generating and amplifying bursts with and without running stabilization and measuring the spectrum of the amplified bursts, since it is sensitive to the intraburst CEPs. During the experiment it was made sure, that the setup is covered in order to omit air disturbances and that the system was already running for some time ($\approx 15-30$ minutes) for achieving thermally stable operation.

Free-running amplification

The free-running spectrum can be seen in Fig. 3.16. The intraburst CEP drift $\delta\phi_{CEP}$, extracted from the spectrum is directly proportional to the cavity detuning drift δL, measured over a time Δt its rate was

$$\frac{\delta\phi_{CEP}}{\Delta t} \approx 37.70\frac{rad}{min}, \tag{3.29}$$

which corresponds, according to $\delta\phi_{CEP} = 2k_0\delta L$ to a cavity detuning drift δL of

$$\boxed{3090.0\frac{nm}{min} \text{ @ } 1030nm}$$

Both, the temporally monotonic behaviour on such a time scale and the magnitude of the drift is consistent with thermal drifts.

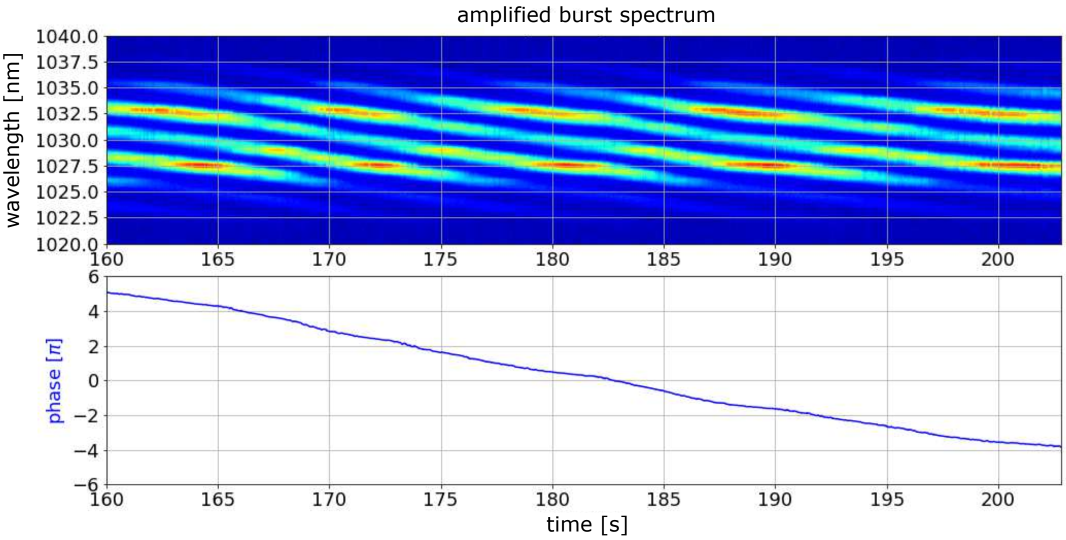

Figure 3.16: Measurement of the free-running, amplified burst spectrum over time: (Top) Spectrum as a colormap of wavelength and time (Bottom) Phase of the interference pattern over time

Phase-stable amplification

A measurement of a phase-stable amplification can be seen in Fig. 3.17. It can be seen, that the reference spectrum is stabilized completely, while for the amplified burst spectrum, there is still some drift, which is

$$\frac{\delta\phi_{CEP}}{\Delta t} \approx 0.16\frac{rad}{min}, \tag{3.30}$$

which corresponds to a cavity detuning drift δL of

$$\boxed{13.11\frac{nm}{min} \text{ @ } 1030nm}$$

This means an about 236 times lower drift, than for the free-running case, which is a tremendous improvement enabling the capability for a number of applications (Chapter 4). The remaining phase-drift may be due to the fact, that the pulses are not reflected from the PZT-driven mirror with an incident angle of 0°, which may have an impact on the RA length and thus, on the cavity detuning. It was seen during the experiment, that the travel range of this mirror definitely has an impact on the output power in this configuration. Looking at the noise spectral density in Fig. 3.18a and the integrated phase noise in Fig. 3.18b, which were retrieved from the development of the phase in Fig. 3.16 for the free-running case and in Fig. 3.17 for the time 200s-700s for the stabilized case, it can be seen that the stabilization reduces the noise throughout the observed frequency range. This is consistent with the sampling rate of the whole system, which was determined to be $\approx 42Hz$. It is expected that optimization of acquisition and control speed will further reduce the slow drift noise below $42Hz$.

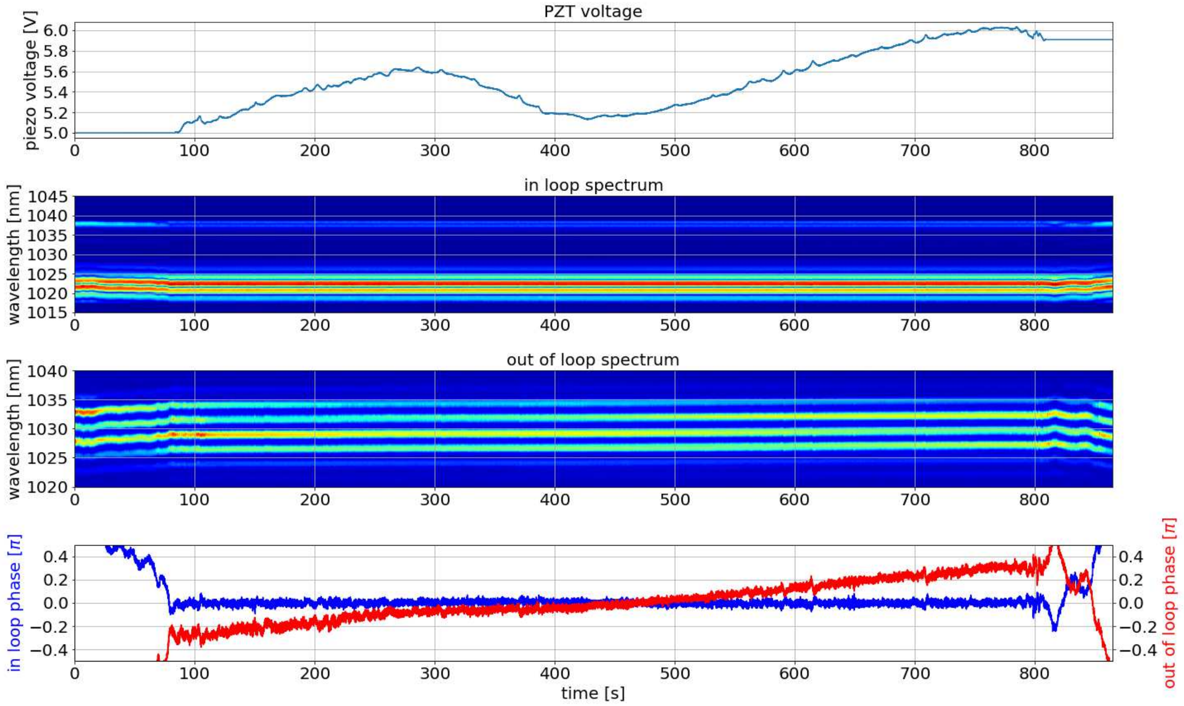

Figure 3.17: Measurement of the phase-stabilized amplified burst spectrum over time. In-loop and out-of-loop refer to reference pulse and amplified burst output spectrum, respectively

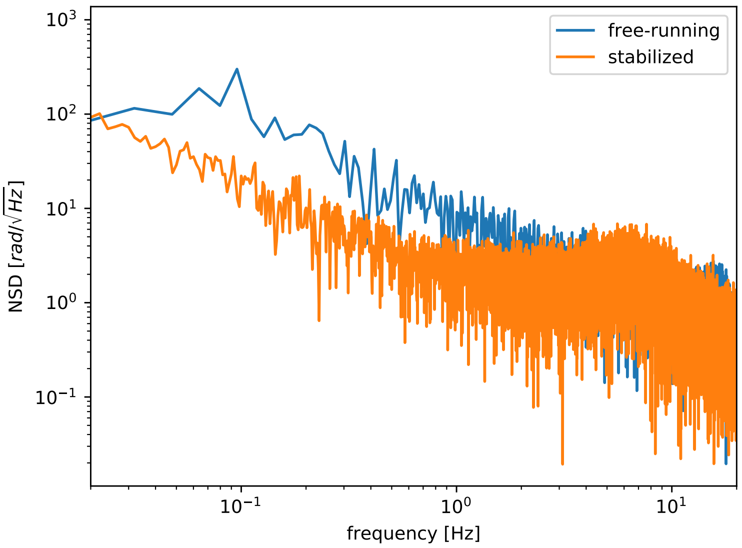

(a)

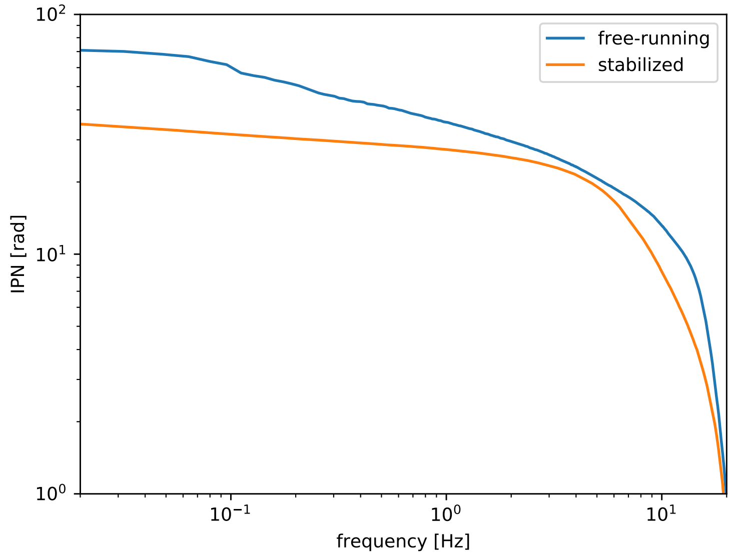

(b)

Figure 3.18: (a) Noise Spectral Density (b) Integrated Phase Noise

3.5.4 Spectral characteristics of phase-locked bursts

An interesting subject are the spectral characteristics of a train of bursts with stabilized intraburst CEPs. When setting the intraburst CEPs to zero (e.g. by an AOM, Sec. 3.2) and using an intraburst CEP stabilization, like in Sec. 3.5.3, it can be assumed that the CEP just varies from burst to burst (Fig. 3.19).

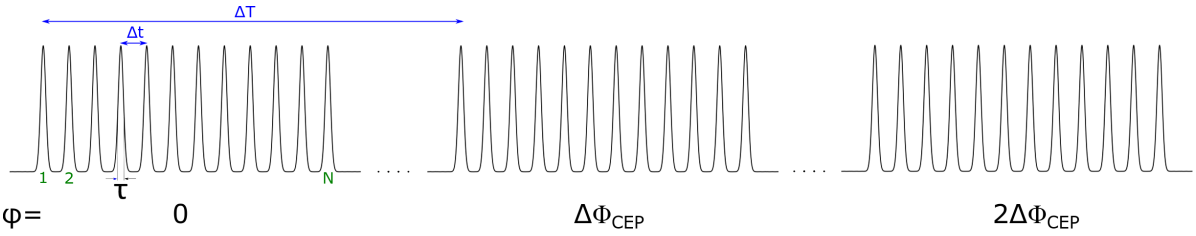

Figure 3.19: Depiction of pulse bursts with pulse spacing Δt, pulse length τ and a CEP shift $\Delta\Phi_{CEP}$ from burst to burst, whereas intraburst CEPs are set to zero

The burst train, consisting of M bursts and N pulses in each burst, can then be formulated as

$$E(t) = \sum_{m=0}^{M-1}\sum_{n=0}^{N-1} E_P(t - n\Delta t - m\Delta T)\exp^{jm\Delta\Phi_{CEP}}, \tag{3.31}$$

with $E_P(t)$ being the waveform of a single pulse. The Fourier-transform of Equ. 3.31 is

$$E(\omega) = \sum_{m=0}^{M-1}\sum_{n=0}^{N-1} E_P(\omega)e^{-jn\Delta t\omega}e^{-jm\Delta T\omega}e^{jm\Delta\Phi_{CEP}} \tag{3.32}$$

$$= E_P(\omega)\sum_{n=0}^{N-1} e^{-jn\Delta t\omega}\sum_{m=0}^{M-1} e^{-jm(\Delta T\omega - \Delta\Phi_{CEP})} \tag{3.33}$$

$$= E_P(\omega)\cdot\frac{1 - e^{-jN\Delta t\omega}}{1 - e^{-j\Delta t\omega}}\cdot\frac{1 - e^{-jM(\Delta T\omega - \Delta\Phi_{CEP})}}{1 - e^{-j(\Delta T\omega - \Delta\Phi_{CEP})}} \tag{3.34}$$

which gives after some calculation

$$E(\omega) = E_P(\omega)\cdot f(\omega; \Delta t, N)\cdot g(\omega; \Delta T, M, \Delta\Phi_{CEP}) \tag{3.35}$$

$$f(\omega; \Delta t, N) = -\frac{\sin(\frac{N\Delta t\omega}{2})}{\sin(\frac{\Delta t\omega}{2})}e^{-j\frac{N-1}{2}\Delta t\omega} \tag{3.36}$$

$$g(\omega; \Delta T, M, \Delta\Phi_{CEP}) = -\frac{\sin\left(\frac{M(\Delta T\omega - \Delta\Phi_{CEP})}{2}\right)}{\sin\left(\frac{\Delta T\omega - \Delta\Phi_{CEP}}{2}\right)}e^{-j\frac{M-1}{2}(\Delta T\omega - \Delta\Phi_{CEP})} \tag{3.37}$$

The first two factors in Equ. 3.35 represent the spectrum of a single burst for $\Delta\phi_{CEP} = 0$, which is the envelope of the spectrum of a train of bursts. Similarly to the single burst case, there is a modulation $g(\omega; \Delta T, M, \Delta\Phi_{CEP})$, which represents the formation of spectral modes. However, in case of a burst train an infinite number of bursts $M \to \infty$ can be assumed, which leads to a comb structure below the envelope (Fig. 3.20). The quantities $\Delta\Omega$, $\Delta\Omega_{zz}$ are still related to pulse number N and pulse spacing Δt according to Eqs. 3.8,3.9, respectively. An interesting fact is, that the CEP-drift $\Delta\Phi_{CEP}$ from burst to burst doesn't affect the envelope, but only the frequency-offset of the combs! These are separated by a frequency

$$\Delta\omega = \frac{2\pi}{\Delta T} = 2\pi f_{rep}, \tag{3.38}$$

which scales with the burst spacing ΔT or the burst repetition rate f_{rep}, which is in the kHz-regime.

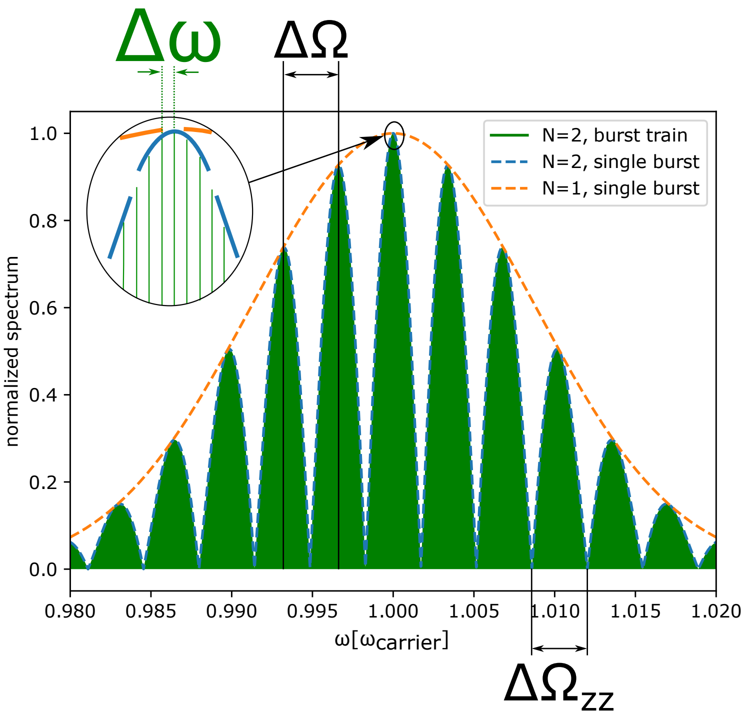

Figure 3.20: Spectrum of a train of bursts with $N = 2$ pulses per burst. The spectra for single pulse and single burst are according Eqs. 3.35-3.37, the comb structure is a depiction

4 Applications

This chapter is devoted to the exploration of possible applications of pulse bursts as generated in course of this thesis. In most of the applications found, bursts already play an important role and enhancement of burst technology, like parameter space, burst reproducibility and stability is expected to contribute strongly to the improvement of respective applications.
First, materials processing is discussed (Sec. 4.1), including micromachining (Sec. 4.1.1) or pulsed laser deposition (Sec. 4.1.2), where bursts with ns pulse spacing are already a standard in industry. Then, a current project in our group is shown, which is the generation of continuously-tunable, narrowband THz pulses (Sec. 4.2). Nonlinear, time-resolved spectroscopy, already a huge field of research, is investigated as a potential application area in Sec. 4.3, covering the recently demonstrated ps pulse spaced single pump - multiple probe technique (Sec. 4.3.1) and comb spectroscopy (Sec. 4.3.2). Finally, a method for quantum control is shown, which is STIRAP (Sec. 4.4) where the achieved phase-stability of bursts is expected to be fruitful.

4.1 Materials Processing

4.1.1 Micromachining

Micromachining, the mechanical processing of materials on the micrometer scale, is a highly important technique for several areas like surgery or industrial materials processing. The superior performance in micromachining of ultrashort laser pulses with pulse durations lower than 1ps compared to picosecond or nanosecond laser pulses is already known for some time [24]. This counts for the use of such pulses for ablating, drilling or cutting of materials on a micrometer scale. Much research effort was already put into the understanding of the physical mechanisms driving the ablation of materials [25, 26]: Ultrashort laser pulses not only allow the processing of conductive materials like metals, but also of semiconductors and insulators due to the interplay of nonlinear processes, which are avalanche ionization and multi-photon ionization, leading to laser-induced breakdown. The laser-induced breakdown sets in as soon as a certain threshold fluence F_{th} of a pulse is reached, where multi-photon absorption starts to become significantly probable, which leads to ionization of deeply bound electrons serving as seed for the subsequent avalanche ionization process. Due to the nonlinear nature of the multi-photon process, the threshold fluence F_{th} is much stronger pronounced and shows deterministic behaviour for ultrashort pulses in opposite to the statistical behaviour of avalanche ionization induced by nanosecond pulses, which lack the multi-photon process and requires defect electrons as avalanche seed.

After deposition of energy in the electronic system of a material by the laser pulse, the heat transfer from electrons to the solid can be explained by a two temperature model [27]. Energy transfer to the lattice, which happens already within the pulse duration, can be faster than thermal diffusion for ultrashort pulses. Thus, the ablated volume is not governed by the diffusion length L_D, but by the absorption depth L_A, which are given by

$$L_D = \sqrt{D \cdot \Delta t} \tag{4.1}$$

$$L_A = \frac{1}{\alpha_I} \tag{4.2}$$

with D being the diffusion coefficient, Δt the pulse length and α_I the intensity-dependent absorption coefficient according to Beer's law, leading to smaller heat-affected zones and direct evaporation of the material. This explains the precision of micromachining with ultrashort pulses.

The behaviour of the damage threshold fluence F_{th} was investigated for multiple ns pulses by Jee et al. [28] who introduced a cumulative equation describing the dependence of damage threshold on the number of pulses:

$$F_{th,M} = F_{th,1} M^{S-1}, \tag{4.3}$$

with M being the number of pulses, $F_{th,M}$ the threshold fluence for M pulses and S the incubation coefficient. The latter represents the cumulative plastic-strain energy, which is stored in the material by the pulse, where a lower value of S with $S < 1$ corresponds to accumulation of energy. Very recently, this model was extended by Gaudiuso et al. [29] for M bursts consisting of N pulses:

$$F_{th,M} = F_{th,1} M^{S_N-1}, \tag{4.4}$$

with S_N being the incubation coefficient, depending on the number N of pulses in a burst. In the same publication a reduction of the incubation coefficient for an increased number of pulses per burst (ps-spaced pulses, 650fs pulse duration, 5-25μJ pulse energy) was shown (Fig. 4.1), which indicates a more efficient deposition of the energy in the material in burst-mode.

The ablation speed is another important criterion for such applications. It can be increased by either higher pulse energy or higher repetition rate. However, for these criteria the shielding effect and heat accumulation need to be considered [30]. The former is caused by a plume of particles ejected from the surface, leading to absorption and scattering of subsequent pulses, while the latter accounts for absorbed energy, which is not transferred to evaporated particles and stays in the irradiated region as heated plasma, because it cannot diffuse out of this region before the next coming pulse arrives on the surface. Thermal transport from plasma to the material increases the temperature of the lattice and can lead to melting, which deteriorates the drill hole quality.

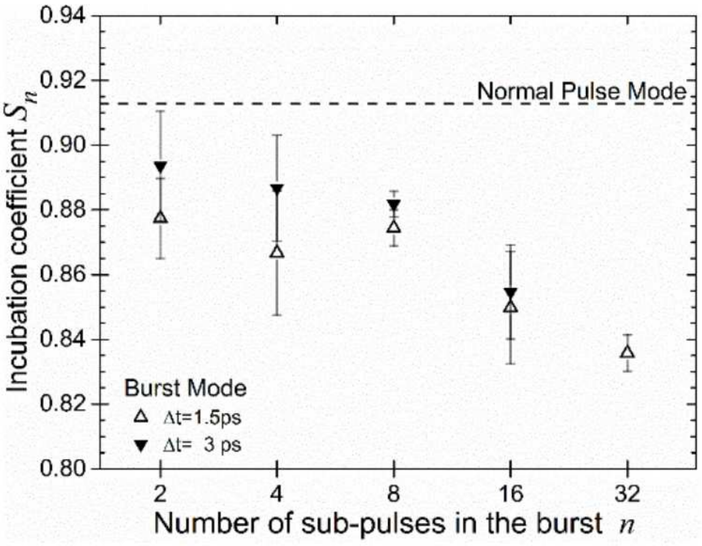

Figure 4.1: *"Incubation coefficient Sn versus the number n of sub-pulses in the burst for the two different time separations, 1.5 and 3 ps. The dashed line represents the incubation coefficient in case of Normal Pulse Mode."*, Figure and description from [29]

Summarized, by increasing the pulse energy, particle shielding becomes stronger, while when increasing the pulse repetition rate, heat accumulation can deteriorate ablation precision.
However, the effects mentioned can be circumvented by utilizing ablation-cooling as shown by Kerse et al. [31]. This process is happening if the pulse separation is smaller than the thermal relaxation time τ_0 of the material, which leads to heat extraction from the lattice by material ablation. In their work [31], this is shown in Cu and Si for pulse repetition rates of about 10MHz. Since the residual heat, which would normally be consumed by melting, is efficiently utilized for ablation, the efficiency of ablation is increased by an order of magnitude, with a three orders of magnitude less required pulse energy.
The scaling of the incubation coefficient S_N with the number of burst pulses and the ablation-cooling effect for pulse repetition rates higher than ≥10MHz, together with the condition of sufficient high pulse fluence $F \geq F_{th}$ even for a high number of pulses per burst, opens up the expectation of superior performance of amplified mJ pulse bursts with a high scalability of the pulse number and a tunable spacing down to below picoseconds compared to usually established sources for such applications. Thus, the investigation of light-matter interactions in this burst-mode regime and applications based on these interactions enabling highly efficient micromachining with high speed is proposed.

4.1.2 Pulsed Laser Deposition (PLD)

The understanding of light-matter interaction with fs pulses described in the last section proved to be useful for Pulsed Laser Deposition (PLD), where the ablated material is used as target material for deposition on a substrate [32]. The suppression of thermal processes in the light-matter interaction avoids the generation of droplets in PLD when using fs pulses. It was demonstrated by Murakami et al. [33] that PLD with fs pulses in burst-mode shows a higher deposition rate compared to a pulse train with the same total number of pulses (0.05 Å/s for normal mode with 1MHz repetition rate, 0.33 Å/s for burst-mode with 10 pulses, 50MHz intraburst frequency and 100kHz burst repetition rate) and a smaller average particle-size of the films. An investigation of dependence of the deposition rate and film morphology on higher intraburst frequencies up to the THz regime would be possible now.

4.2 Generation of continuously-tunable, narrowband THz pulses

A specific application of femtosecond pulse bursts is currently investigated in our group, which is the generation of continuously-tunable, narrowband THz pulses. The experimental setup can be seen in Fig. 4.2.

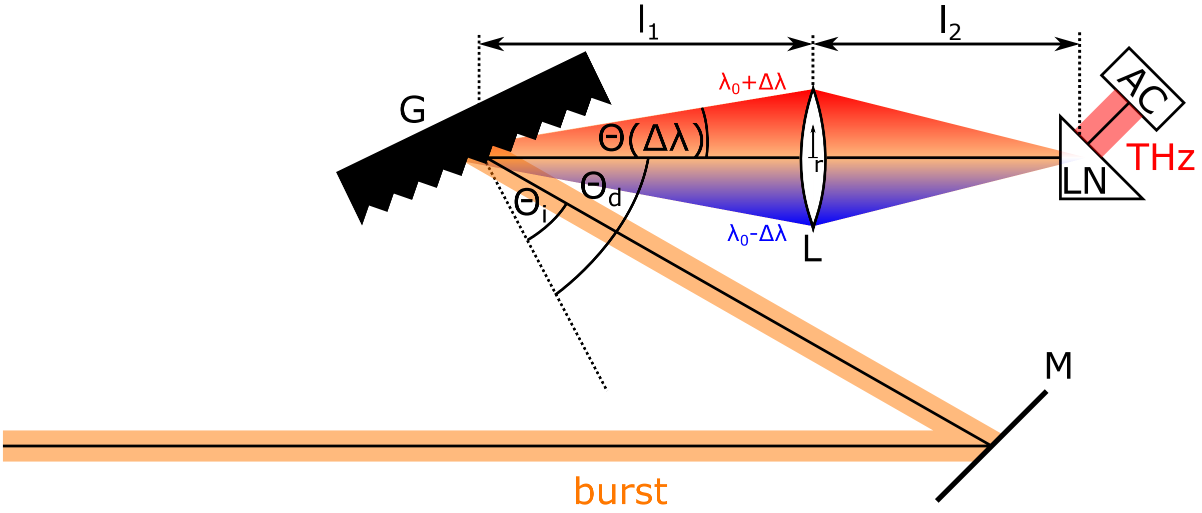

Figure 4.2: Experimental setup for the generation of continuously-tunable, narrowband THz-pulses

A mirror M directs the bursts on a grating G, where they are diffracted according to the diffraction law for reflection-gratings

$$\sin(\Theta_i) + \sin(\Theta_m) = mn\lambda, \tag{4.5}$$

with Θ_i, Θ_m being the incidence and order-m diffraction angle, respectively, n the line density of the grating, m the diffraction order and λ the wavelength. The reason for using a grating is to tilt the pulse front, which provides a much higher efficiency for THz generation due to phase-matching. For the experiment, the order $m = 1$ is used. Subsequently, the diffracted beam is focussed on a Lithiumniobat-crystal (LN) by a lens (L). The bursts are optically rectified by the crystal's nonlinear response, leading to single THz pulses, which are measured by an autocorrelator (AC). In Fig. 4.2, also the dispersion of the diffraction is depicted. The angles were $\Theta_i = 37°$ and $\Theta_d = 57°$.
The results for the THz pulses generated by the optical rectification of fs pulse bursts with a pulse spacing of $3ps$ are shown in the case of non-phase-locked bursts (Fig. 4.3). The spectrum shows a clear narrowband signal at the tunable intraburst frequency $f_{THz} = 1/\Delta t$. However, strong background noise in the remaining spectrum can be seen, which can be explained as follows: Because of a broadening of the pulses, the individual pulses were stretched to around $20ps$, which is much longer than the pulse spacing of $3ps$. Thus, the pulses in the burst were overlapping and since they were not phase-locked, the spectrum of the whole burst was not stable and corrupted by phase-noise. This shows an example for the motivation of generating phase-locked bursts. In order to understand this process more deeply, the pulse broadening mechanism is investigated in course of this work in chapter 5, both experimentally and theoretically.

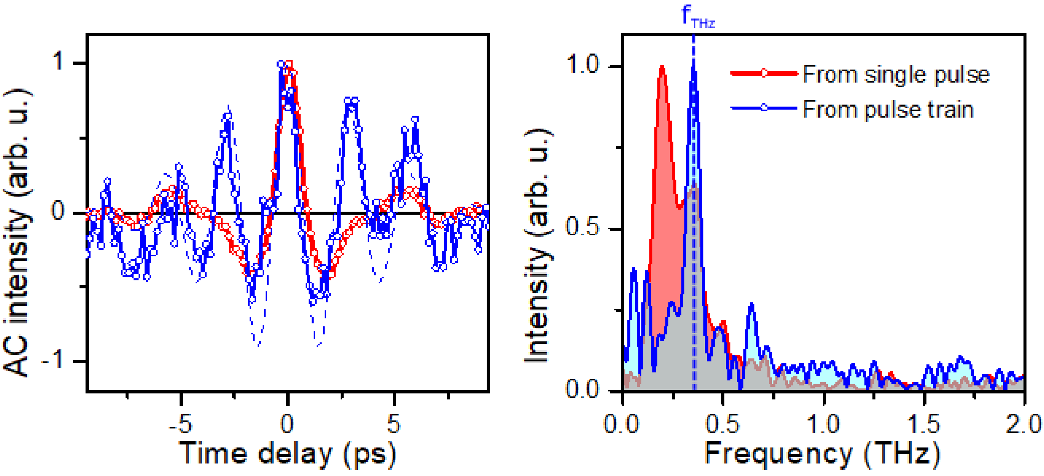

Figure 4.3: Measurement results for the THz-pulses generated by optical rectification of fs non-phase-locked pulse bursts with $N = 4$ pulses and a pulse spacing of $3ps$: (Red) Single pulse (Blue) Pulse burst/train a) Autocorrelation trace b) Spectrum, showing a narrowband signal at the intraburst frequency f_{THz}

4.3 Nonlinear spectroscopy

4.3.1 Single pump - multiple probe

Pump-probe spectroscopy, already invented in the 19th century by August Toepler for investigating the propagation of sound waves in optical glasses [34], is a powerful technique when applied with ultrashort laser pulses enabling the study of ultrafast dynamics in atomic [35–37], molecular [38] and solid-state [39] systems. The principle comprises a pump pulse, which initiates the dynamic in a system and a probe pulse, which analyzes the dynamical behaviour of the system over time by varying the time-delay between pump- and probe-pulse. Pulse bursts can extend this technique: By using the first pulse in the burst as pump-pulse and the following pulses as probe, single pump - multiple probe spectroscopy can be realized. This was already demonstrated by David et al. [40] by splitting an X-ray pulse with gratings into multiple pulses and recombining the delayed pulses at a sample. The delay is defined by the geometry of the setup and can be accurately set by this method up to $\approx 1ps$ with an uncertainty of 0.4%. Demultiplexing of the burst into individual probe pulses after interaction with the sample happens naturally, since the pulses are directed on the sample at different angles. This demonstration shows the possibility of single pump - multiple probe experiments, enabling the observation of ultrafast irreversible processes and with single-shot pump-probe spectroscopy strongly reducing measurement time. The performance of burst with tunable sub-picosecond spaced and highly scalable pulses with sufficient energy indicates a strong utility for such a technique for nonlinear, time-resolved spectroscopy.

4.3.2 Frequency Comb Spectroscopy

The possibility to generate frequency combs in the optical regime enabled measurements in the frequency domain with unprecedented accuracy, leading to the award of the Nobel Prize 2005 to Hall and Hänsch [41]. This is achieved by controlling and stabilizing the CE frequency f_{CE} and the repetition rate f_r of a frequency comb. The technique can be extended by using two frequency combs with a slight difference Δf_r in repetition rate [42]. Dual-Comb Spectroscopy allows measuring single-shot spectra with unprecedented accuracy and SNR. As can be seen in Fig. 3.20, the envelope of the spectrum of a train of bursts (dashed blue in Fig. 3.20) is similar to a comb structure. The intraburst CEP stabilization stabilizes the comb, the width and distances between comb modes are given by Eqs. 3.8,3.9 and the offset can be set by the control of intraburst CEPs. The mode width is indirectly proportional to the burst duration $N \cdot \Delta t$, which is the product of the number of pulses N and the pulse spacing Δt. However, the burst duration is restricted according to Equ. 2.10. For example, for a cavity with 3m length and a burst with a pulse spacing of 1ps, the pulse number would be limited to 20000, which would correspond to a mode width of 100MHz. This is comparable to the resolution of mutually coherent dual-combs [42]. The spectral resolution can be good enough for various molecular or solid-state systems and the high-intensity of fs pulse bursts opens up the access to nonlinear optical techniques, like frequency conversion. As can be seen in [42], there is a huge lack of dual-combs in several spectral regimes, which would be accessible with frequency conversion techniques. Additionally, measurements with high intensity would improve strongly the SNR, thus avoiding the needs for techniques like cavity enhancement or cavity ring-down spectroscopy [43, 44]. The high intraburst frequency would prove as an advantage even in the IR: The optical spectrum is translated into an RF spectrum with a compression factor m given by

$$m = \frac{f_r}{\Delta f_r}. \tag{4.6}$$

So, if the repetition rate f_r can be above 1THz, the frequency detuning Δf_r can also be set higher while keeping the compression factor m constant. The minimum time t_{min}, which is needed to resolve the whole RF spectrum is given by

$$t_{min} = \frac{1}{\Delta f_r}. \tag{4.7}$$

Therefore, with a higher frequency detuning Δf_r, the minimum resolving time is reduced. A proposed way how to produce coherent phase-locked amplified fs dual-comb bursts with the Vernier effect can be seen in Fig. 4.4. The pulses can be picked alternately from the same oscillator and sent to two separate phase-stable Vernier amplifiers, which are as described in chapter 3. The intraburst CEPs $\phi_{i1,1}, \phi_{i1,2}$ of the comb bursts can be given as input to the amplifiers for the internal AOMs.

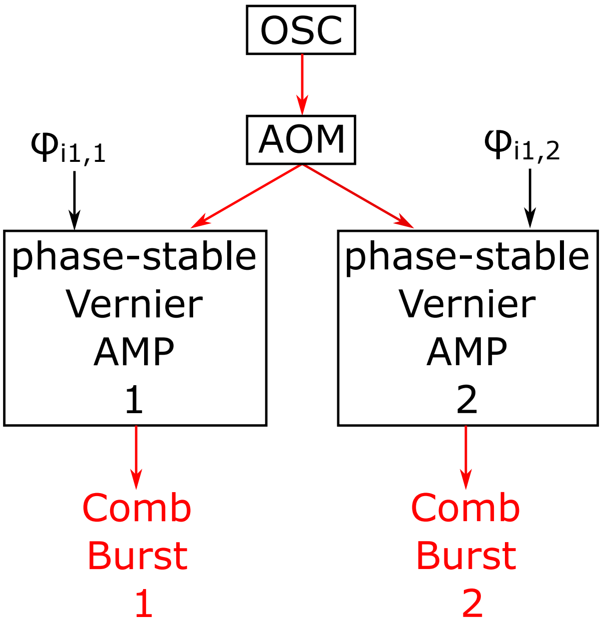

Figure 4.4: Proposed concept for the generation of pairs of amplified femtosecond frequency comb bursts with THz intraburst frequency

4.4 Quantum control - STIRAP

In order to control quantum systems properly, one needs to be able to fully transfer population between quantum states with robust methods to satisfy real-world conditions which are met in the laboratory, like variable pulse shape or intensity. One such method is stimulated rapid adiabatic passage (STIRAP), which uses pulse sequences for transferring population from a state 1 to another state 3 [45] (Fig. 4.5). The process is linked over a state 2, which however is not populated during the transfer process. Originally, it was shown that efficient STIRAP can just be poorly achieved when using pulses, which are shorter than about 1ns [46], because they don't fulfill the adiabaticity criterion. However, Shapiro et al. [47] demonstrated efficient STIRAP with a burst of sub-ps spaced femtosecond pulses for the transition $5s_{1/2} \Rightarrow 5p_{1/2}$ in ^{85}Rb. This technique is defined as piecewise adiabatic passage (PAP) [48]. In this work, a SLM was used for burst formation limitating the number of pulses. Femtosecond bursts with a highly scalable pulse number and individual pulse parameter tuning would be perfectly suitable for PAP, indicating the potential of extraordinary control of quantum systems and dynamics.

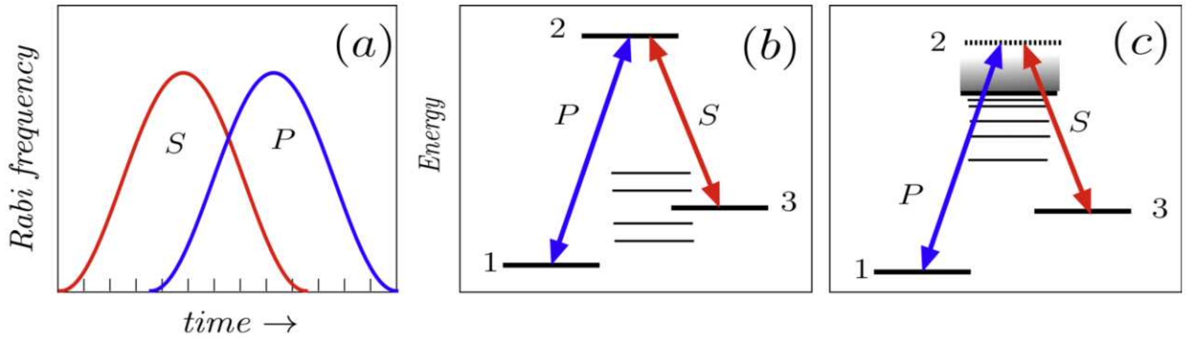

Figure 4.5: *"Pulse sequences and linkages. (a) Schematic of timing for S and P Rabi-frequency-pulses of STIRAP. (b) Lambda linkage pattern for tradi- tional STIRAP. State 1 is initially popu- lated. Two-photon resonance conditions have selected target state 3 from neigh- boring alternatives. (c) Continuum STI- RAP, with linkage through a continuum of intermediate states"*, Figure and description from [45]

5 Pulse broadening mechanism for the generation of continuously-tunable, narrowband THz pulses

In this chapter, the pulse broadening, which is happening when generating continuously-tunable, narrowband THz pulses with fs pulse bursts is investigated. In the setup, the combination of grating and lens are the cause for the strong temporal broadening of the pulses. Pulse broadening mechanisms are angular dispersion broadening (Sec. 5.1) and pulse tilt broadening (Sec. 5.2), for both of which an analytic model will be formulated. A combined model is explained in Sec. 5.3. Experimental results from the measurement of pulse broadening will be shown and a comparison with simulations based on the formulated models will be done in Sec. 5.5.

5.1 Dispersion broadening

As can be seen from Equ. 4.5 and in Fig. 4.2, the grating imposes angular dispersion on the pulse. In combination with the lens with focal distance f, this leads to a spectral optical path difference

$$\Delta s(\Delta\lambda) = \Delta s_{grating}(\Delta\lambda) + \Delta s_{lens}(\Delta\lambda) \tag{5.1}$$

$$\Delta s_{grating}(\Delta\lambda) = \frac{l_1}{\cos(\Theta(\Delta\lambda))} + \sqrt{(\tan(\Theta(\Delta\lambda))l_1)^2 + l_2^2} \tag{5.2}$$

$$\Delta s_{lens}(\Delta\lambda) = \frac{-r(\Theta(\Delta\lambda))^2}{2f} \tag{5.3}$$

where $\Delta s_{grating}$ is the optical path difference coming from the angular dispersion and Δs_{lens} the optical path difference introduced by the lens, approximated as thin, parabolic lens. The quantities in Eqs. 5.1-5.3 are as depicted in Fig. 4.2, $\Theta(\Delta\lambda)$ according to Equ. 4.5 and $\Delta\lambda = \lambda - \lambda_0$. With the dispersion relation

$$k(\omega) = \frac{2\pi}{\lambda(\omega)} \tag{5.4}$$

$$\Delta\lambda(\omega) = \lambda(\omega) - \lambda_0 = \frac{2\pi c_0}{\omega} - \frac{2\pi c_0}{\omega_0} \tag{5.5}$$

this leads to a spectral phase modulation of

$$E'(\omega) = E(\omega) \cdot e^{jk(\omega)\Delta s(\omega)}. \tag{5.6}$$

This spectral phase modulation leads to deformation and broadening of the pulse, as can be shown in Sec. 5.5.

5.2 Pulse tilt broadening

Differently from reflection, the front of a pulse with diameter d_i is tilted with respect to the direction of propagation under diffraction, which is a purely geometric effect arising from the diffraction law (Equ. 4.5). This is, because those parts of the pulse front, which arrive later at the grating, have to travel a longer optical path compared to the parts arriving earlier.

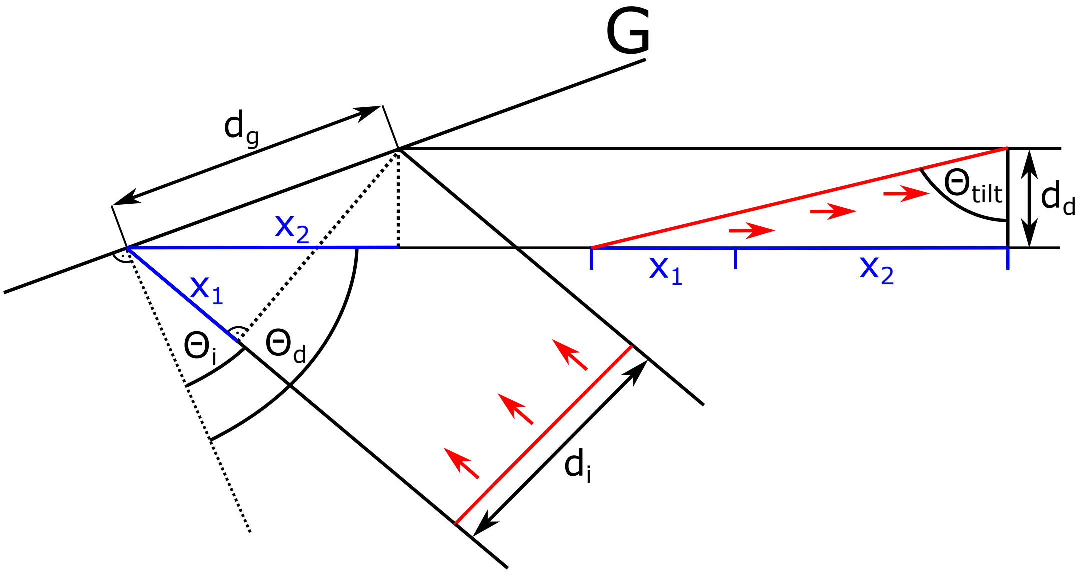

Figure 5.1: Depiction of the pulse front tilt Θ_{tilt} due to the diffraction on the grating: (Red) Pulse front (Blue) Maximum optical path difference $x_1 + x_2$

From Fig. 5.1 following relations can be seen:

$$d_g = \frac{d_i}{\cos(\Theta_i)} = \frac{d_d}{\cos(\Theta_d)} \tag{5.7}$$

$$x_1 = d_i \tan(\Theta_i) \tag{5.8}$$

$$x_2 = d_d \tan(\Theta_d) \tag{5.9}$$

$$\tan(\Theta_{tilt}) = \frac{x_1 + x_2}{d_d} = \frac{\sin(\Theta_i) + \sin(\Theta_d)}{\cos(\Theta_d)} \tag{5.10}$$

If the tilted pulse is subsequently focussed by the lens, it projects this tilt on the optical axis at its focus, which leads to a pulse duration (FWHM) $\tau_{tilt,FWHM}$ of

$$\tau_{tilt,FWHM} = \frac{d_{d,FWHM}\tan(\Theta_{tilt})}{c_0} \tag{5.11}$$

$$= \frac{d_{i,FWHM}}{c_0} \cdot \frac{\sin(\Theta_i)+\sin(\Theta_d)}{\cos(\Theta_i)}, \tag{5.12}$$

which can be much longer, than the pulse duration of the non-tilted pulse.

5.3 Combined model of angular dispersion and pulse tilt

In order to compare the theory of Secs. 5.1,5.2 with the measurement, a combined model of angular dispersion and pulse tilt needs to be formulated. The temporally broadened pulse in the focus $E_{broadened}(t)$ can be composed of an infinite number of partial waves $E_L(r,t)$ coming from the lens L, parametrized by its radial coordinate r (Fig. 4.2)

$$E_{broadened}(t) = \int_{-r_L}^{r_L} E_L(r,t)dr \approx \int_{-\infty}^{\infty} A(r)e_L(r,t)dr \tag{5.13}$$

$$A(r) = \exp\left(-4\ln(2)\left(\frac{r}{2r_d}\right)^2\right), \tag{5.14}$$

where r_L is the radius of the lens, r_d the radius of the tilted pulse and $A(r)$ the spatial envelope due to the transverse beam profile. The integral limits could be set to infinity because of the finite support of $A(r)$. The effect of the pulse tilt can be included by mapping the radial coordinate at the lens r with the temporal delay due to the pulse tilt τ_{tilt}

$$r = \frac{c_0\tau_{tilt}}{\tan(\Theta_{tilt}(\omega))} \approx \frac{c_0\tau_{tilt}}{\tan(\Theta_{tilt}(\omega_0))}, \tag{5.15}$$

with Θ_{tilt} being the tilting-angle as depicted in Fig. 5.1, which is frequency-dependent due to angular dispersion Eqs. 4.5,5.7-5.10 and, as first approximation, can be taken constant with the value corresponding to the frequency ω_0 of the center wavelength of $1030nm$. Therefore, the integral of Equ. 5.14 can be changed into

$$E_{broadened}(t) = \frac{c_0}{\tan(\theta_{tilt,0})}\int_{-\infty}^{\infty} A(r(\tau))e_L(r=0,t-\tau)d\tau, \tag{5.16}$$

where the approximation

$$e_L(r(\tau),t) \approx e_L(r=0,t-\tau) \tag{5.17}$$

was made, which is valid if the phase shift of angular dispersion does not depend on the radial coordinate r in the region $r < r_d$, where $A(r)$ is substantially higher than zero. Actually, the pulse tilt happens along the pulse diameter, which is $d_{d,FWHM} = 2.412mm$ for the center wavelength of $1030nm$. This can be compared to the diameter at the lens induced by angular dispersion: For a pulse with wavelengths from $1026nm$ to $1034nm$, the angular dispersion leads to a divergence $\Theta(\Delta\lambda)$ of 0.587° and 0.596° resulting in a pulse diameter of $27.06mm$ at the lens. Thus, justifying the calculation as first approximation. The angular dispersion can be taken into account by Equ. 5.6 such that

$$e_L(r=0,t) = FT^{-1}\left(e^{jk(\omega)\Delta s(\omega)}e_{in}(\omega)\right), \tag{5.18}$$

with FT^{-1} being the inverse Fourier-transformation, $\Delta s(\omega)$ the spectral optical path difference according to Eqs. 5.1-5.3 and $e_{in}(\omega)$ the spectral input pulse. For the simulation, these formulas where used together with a Gaussian input pulse with a central wavelength of $\lambda_0 = 1030nm$ and bandwidth $\Delta\lambda_{FWHM} = 8nm$.

5.4 Pulse Broadening Measurement

The pulse duration τ_{FHWM} was measured with a single input pulse and by cross-correlation of the diffracted and the non-diffracted pulse (Fig. 5.2). It was taken care that the BBO crystal, in which the cross-correlation was done, was put directly in the focus of the non-diffracted beam focussing lens (L1). Afterwards, the cross-correlation signal (X) was focussed into a spectrometer (SPEC).

A SHG-FROG measurement of the input pulse was done, whose envelope can be seen in Fig. 5.3a. The input pulse duration was about $200fs$ and its horizontal beam diameter $d_{i,FWHM}$ was measured by a beam profiler to be $3.5359mm$ (Fig. 5.3b), which corresponds to a diffracted beam diameter $d_{d,FWHM} = 2.41135mm$ (Equ. 5.7). The angles were $\Theta_i = 37°$ and $\Theta_d = 57°$.

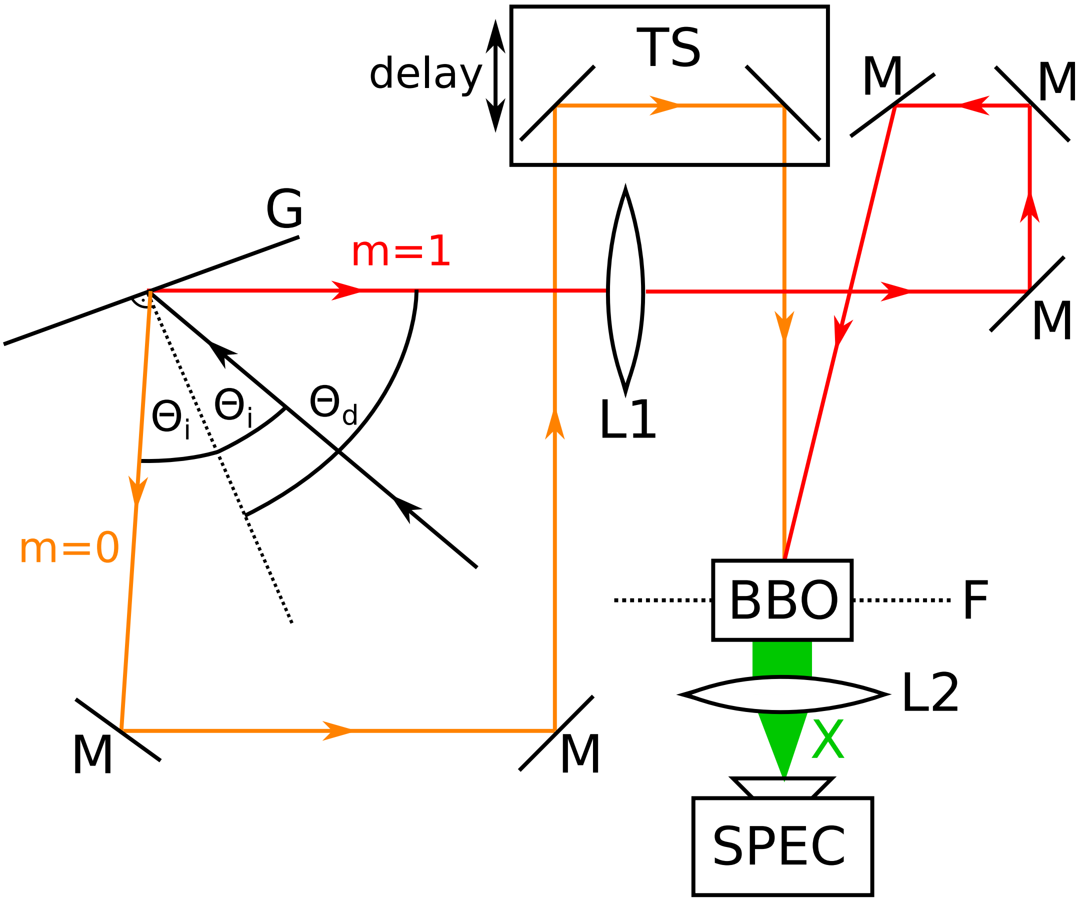

Figure 5.2: Measurement of the pulse broadening by cross-correlating (red) the diffracted beam with (orange) the undiffracted beam in a BBO crystal, which lies in the focal plane F of a lens L1. The cross-correlation signal X (green) is focussed by a lens L2 on a spectrometer SPEC. The delay is set by a translation stage TS.

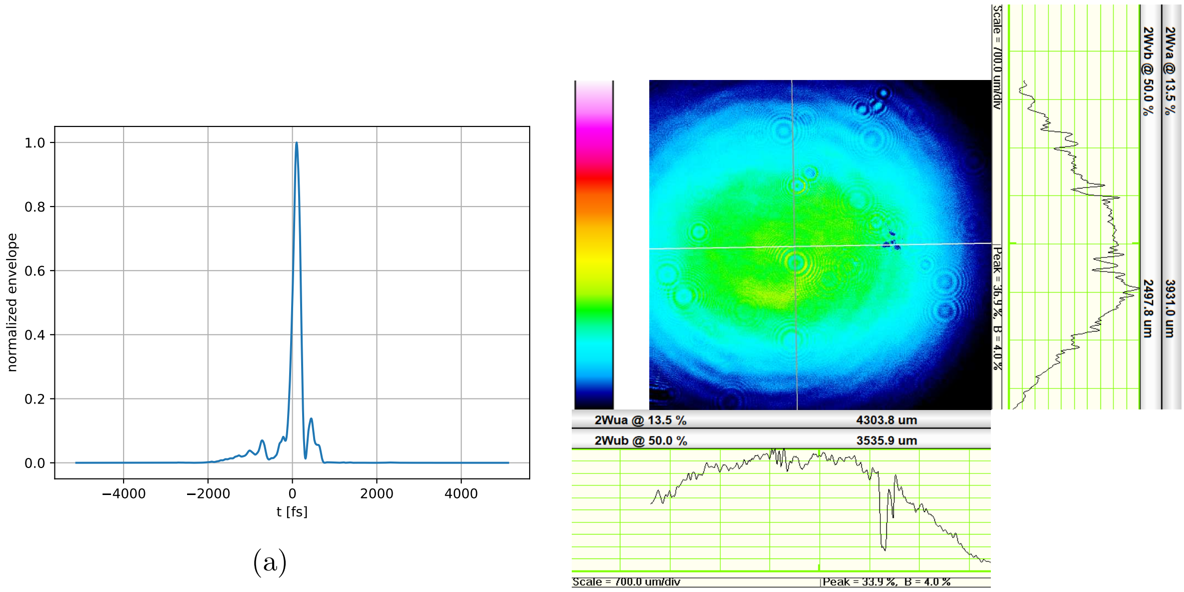

(a)

(b)

Figure 5.3: Characterization of the input pulse for the cross-correlation measurement: (a) Envelope measured with SHG-FROG (b) Pulse shape measured with a beam profiler

5.5 Pulse Broadening Results

The results of the measurement can be seen in Fig. 5.5. The influence of pulse tilt and angular dispersion to the broadening of the pulse can be seen in the results of the simulation (Fig. 5.4). In Tab. 5.1, a comparison of the simulation and the measurement regarding pulse duration can be seen.

	angular dispersion	tilt	angular dispersion & tilt	measurement
$t_1[ps]$	-3.586	-10.580	-10.681	-11.817
$t_2[ps]$	3.308	10.581	10.480	10.615
$\Delta\tau$ (FWHM)	6.894	21.161	21.161	22.432

Table 5.1: Comparison of simulation and measurement results regarding pulse duration: t_1, t_2...pulse FWHM times, $\Delta\tau$ (FWHM) $= t_2 - t_1$ ...FWHM pulse duration

The temporal pulse broadening is well predicted by the model as can be seen by comparison with the FWHM pulse duration of the measured pulse and the simulated Gaussian pulse in Tab. 5.1 and in Fig. 5.5b. The pulse tilt broadening is dominating the pulse broadening process by far. However, even without the pulse tilt broadening, the angular dispersion would broaden the pulse wide enough, such that pulses would already overlap in a burst with $\approx 3ps$ pulse spacing. The angular dispersion imposes a strong chirp on the pulse (Fig. 5.4a), whereas the pulse tilt (Fig. 5.4b) does not. It is interesting to see, that the pulse tilt leads to a strong reduction of chirp introduced by angular dispersion (Fig. 5.4c). Another property of the angular dispersed pulse is the asymmetry of rising- and trailing-edge of the pulse, where the latter is steeper. The steepness of the trailing edge was stronger in the measurement compared to the simulation, while the falling edge could be reproduced well.

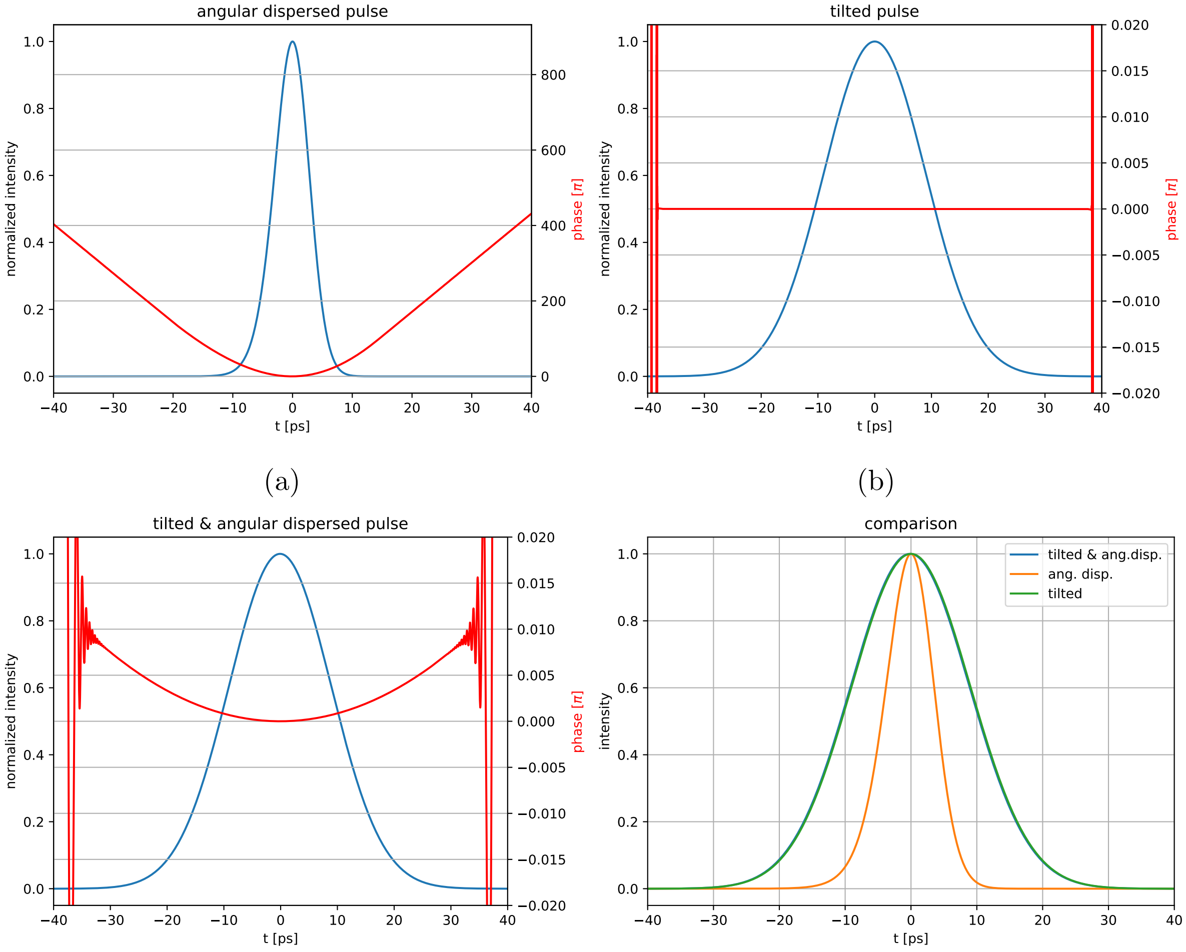

(a)

(b)

(c)

(d)

Figure 5.4: Numerical simulations of the pulse broadening: (a) Dispersion broadened pulse b) Tilt broadened pulse c) Dispersion- and tilt broadened pulse d) Comparison of (a), (b) and (c)

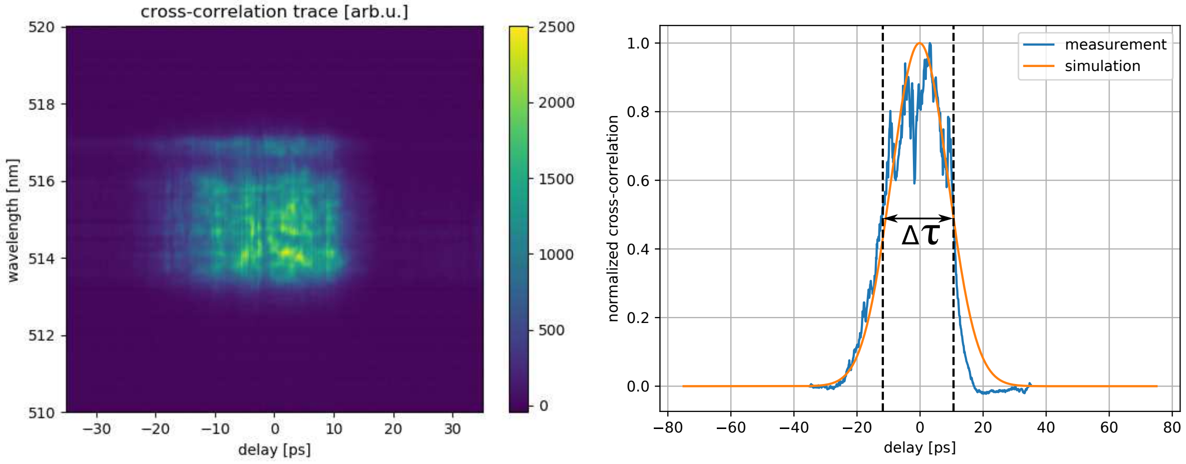

(a) (b)

Figure 5.5: Results of the cross-correlation measurement: (a) Cross-correlation trace b) Cross-correlation

6 Conclusions

The lack of possibilities for generating stable femtosecond pulse bursts with full control over burst parameters over a wide range motivated the effort to develop a novel laser source filling this technological hole. With focus on the control and stabilization of intraburst CEPs, the generation and amplification of bursts with unprecedented properties was shown. The high amplification up to the mJ regime is made possible with the presented phase scrambling technique, which avoids the formation of strong spectral modes, while the reproducibility of bursts was achieved with intraburst CEP stabilization. Both techniques were tested successfully, as was demonstrated with satisfying results. Motivated by developing a novel continuously-tunable narrowband THz source, a pulse broadening mechanism arising during the THz generation process was investigated. For this, a theoretical model of the pulse broadening process was formulated and compared with experimental measurements, which confirmed the theoretical assumptions. A wide range of further potential applications of the generated bursts was revealed which includes material processing, nonlinear spectroscopy and a technique for quantum control. Therefore, an outlook for future developments is given, which shows that the generation, amplification and control of femtosecond bursts can be seen as an important starting point for the technological progress in those fields.

Bibliography

[1] F. Krausz and T. Brabec. Intense few-cycle laser fields: Frontiers of nonlinear optics. *Rev. Mod. Phys.*, 72:545–591, 2000.

[2] F. Krausz. The birth of attosecond physics and its coming of age. *Phys. Scr.*, 91:1–12, 2016.

[3] P. Wu, W.R. Lempert, and R.B. Miles. Mhz pulse-burst laser system and visualization of shock-wave boundary-layer inter- action in a mach 2.5 wind tunnel. *AIAAJ*, 38:672–679, 2000.

[4] B. Thurow, N. Jiang, M. Samimy, and W. Lempert. Narrow-linewidth megahertz-rate pulse-burst laser for high-speed flow diagnostics. *Applied Optics*, 43:5064–5073, 2004.

[5] B. Thurow and A. Satija. A design of mhz repetition rate pulse burst laser system at auburn university. *44th AIAA Aerospace Sciences Meeting*, 2006.

[6] B. Xia and L. Chen. A direct temporal domain approach for pulse-repetition rate multiplication with arbitrary envelope shaping. *IEEE J. Sel. Top. Quantum Electron.*, 11:165–172, 2005.

[7] C. Froehly, B. Colombeau, and M. Vampuoille. Shaping and analysis of picosecond light pulses. *Progress in Optics*, 20:63–153, 1983.

[8] A. Weiner. Femtosecond optical pulse shaping and processing. *Prog. Quantum Electron.*, 19:161–237, 1995.

[9] A.M. Weiner. Femtosecond pulse shaping using spatial light modulators. *Rev. Sci. Instrum.*, 71:1929–1960, 2000.

[10] T. Kurokawa, H. Tsuda, K. Okamoto, K. Naganuma, H. Tenouchi, Y. Inoue, and M. Ishii. Time-space-conversion optical signal processing using arrayed-waveguide gratings. *Electronics Letters*, 33(22):1890–1891, 1997.

[11] A.M. Weiner and D.E. Leaird. Generation of therahertz-rate trains of femtosecond pulses by phase-only filtering. *Optics Letters*, 15(1):51–53, 1990.

[12] D.E. Leaird, S. Shen, A.M. Weiner, A. Sugita, S. Kamei, M. Ishii, and K. Okamoto. Generation of high-repetition-rate wdm pulse trains from an arrayed-waveguide grating. *IEEE Photon. Technol. Lett.*, 13(3):221–223, 2001.

[13] D.E. Leaird, A. M. Weiner, S. Kamei, M. Ishii, A. Sugita, and K. Okamoto. Generation of flat-topped 500-ghz pulse bursts using loss engineered arrayed waveguide gratings. *IEEE Photon. Technol. Lett.*, 14(6):816–818, 2002.

[14] D. Leiard and A. Weiner. Femtosecond direct space-to-time pulse shaping in an integrated-optic configuration. *IEEE J. Quantum Electron.*, 37:494–504, 2004.

[15] J. Azaña and M. A. Muriel. Technique for multiplying the repetition rates of periodic trains of pulses by means of a temporal self-imaging effect in chirped fiber gratings. *Optics Letters*, 24:1672, 1999.

[16] J. Azaña, R. Slavík, P. Kockaert, L. R. Chen, and S. LaRochelle. Generation of customized ultrahigh repetition rate pulse sequences using superimposed fiber bragg gratings. *J. Lightwave Technol.*, 21:1490–1498, 2003.

[17] M.A. Preciado and M.A. Muriel. Proposed flat-topped pulses bursts generation using all-pass multi-cavity structures. *Optics Express*, 17:13875–13880, 2009.

[18] B. Dromey, M. Zepf, M. Landreman, K. O'keeffe, T. Robinson, and S.M. Hooker. Generation of a train of ultrashort pulses from a compact birefringent crystal array. *Appl. Opt.*, 46:5142–5146, 2007.

[19] K. Tai, A. Tomita, J. L. Jewell, and A. Hasegawa. Generation of subpicosecond solitonlike optical pulses at 0.3 thz repetition rate by induced modulational instability. *Appl. Phys. Lett.*, 49:236–238, 1986.

[20] K. and Butkus V. Barkauskas, M. and Neimontas. Device and method for generation of high repetition rate laser pulse bursts, November 2018. WO Patent 2018207042, UK Patent 2562236.

[21] A. S. Hosseini, P. R. Herman, and T. H. Bergmann. Generation of burst of laser pulses, 2008. US Patent US20110182306A1, EP Patent EP2250714B1, WO Patent WO2009103313A1.

[22] N. C. Kothari. Theory of modulational instability in optical fibers. *Optics Communications*, 62(4):247–249, 1987.

[23] D. Strickland and G. Mourou. Compression of amplified chirped optical pulses. *Optics Communications*, 56:219–221, 1985.

[24] B.N. Chichkov, C. Momma, S. Nolte, F. von Alvensleben, and A. Tünnermann. Femtosecond, picosecond and nanosecond laser ablation of solids. *Appl. Phys. A*, 63:109–115, 1996.

[25] X. Liu, D. Du, and G. Mourou. Laser ablation and micromachining with ultrashort laser pulses. *IEEE J. Quantum Electron.*, 33(10):1706–1716, 1997.

[26] M. D. Shirk and P. A. Molian. A review of ultrashort pulsed laser ablation of materials. *J. Laser Appl.*, 10(1):18–28, 1998.

[27] P. P. Pronko, P. A. VanRompay, R. K. Singh, F. Qian, D. Du, and X. Liu. Laser induced avalanche ionization and electron-lattice heating of silicon with intense near ir femtosecond pulses. *MRS Proc.*, 397:45–51, 1996.

[28] Y. Jee, M. F. Becker, and R. M. Walser. Laser-induced damage on single-crystal metal surfaces. *J. Opt. Soc. Am. B*, 5(3):648–659, 1988.

[29] C. Gaudiuso, G. Giannuzzi, A. Volpe, P. M. Lugarà, I. Choquet, and A. Ancona. Incubation during laser ablation with bursts of femtosecond pulses with picosecond delays. *Optics Express*, 26(4):3801–3813, 2018.

[30] A. Ancona, F. Röser, K. Rademaker, J. Limpert, S. Nolte, and A. Tünnermann. High speed laser drilling of metals using a high repetition rate, high average power ultrafast fiber cpa system. *Optics Express*, 16(12):8958–8968, 2008.

[31] C. Kerse et al. Ablation-cooled material removal with ultrafast bursts of pulses. *Nature*, 537:84–88, 2016.

[32] Wikipedia: Pulsed laser deposition. `https://en.wikipedia.org/wiki/Pulsed_laser_deposition`. Accessed: 2019-09-04.

[33] M. Murakami, B. Liu, Z. Hu, Z. Liu, Y. Uehara, and Y. Che. Burst-mode femtosecond pulsed laser deposition for control of thin film morphology and material ablation. *Appl. Phys. Express*, 2, 2009.

[34] P. Krehl and S. Engemann. August toepler - the first who visualized shock waves. *Shock Waves*, 5:1–18, 1995.

[35] M. Chini, K. Zhao, and Z. Chang. The generation, characterization and applications of broadband isolated attosecond pulses. *Nat. Photonics*, 8:178–186, 2014.

[36] F. Lépine, M.Y. Ivanov, and M. J. J. Vrakking. Attosecond molecular dynamics: fact of fiction? *Nat. Photonics*, 8:195–204, 2014.

[37] F. Krausz and M. I. Stockman. Attosecond metrology: from electron capture to future signal processing. *Nat. Photonics*, 8:205–213, 2014.

[38] Ahmed H. Zewail. Femtochemistry: Atomic-scale dynamics of the chemical bond. *J. Phys. Chem. A*, 104:5660–5694, 2000.

[39] A. Schiffrin et al. Optical-field-induced current in dielectrics. *Nature*, 493:70–74, 2013.

[40] C. David, P. Karvinen, and M. et al Sikorski. Following the dynamics of matter with femtosecond precision using the x-ray streaking method. *Scientific Reports*, 5(7644), 2015.

[41] T. Hänsch. Nobel lecture: Passion for precision. *Rev. Mod. Phys.*, 78:1297–1309, 2006.

[42] I. Coddington, N. Newbury, and W. Swann. Dual-comb spectroscopy. *Optica*, 3(4):414–426, 2016.

[43] B. Bernhardt et al. Cavity-enhanced dual-comb spectroscopy. *Nature Photonics*, 4:55–57, 2010.

[44] G. Berden, R. Peeters, and G. Meijer. Cavity ring-down spectroscopy: Experimental schemes and applications. *Int. Rev. Phys. Chem.*, 19:565–607, 2000.

[45] K. Bergmann, N. V. Vitanov, and B. W. Shore. Perspective: Stimulated raman adiabatic passage: The status after 25 years. *J. Chem. Phys.*, 142(170901), 2015.

[46] A. Kuhn, G. W. Coulston, G. Z. He, S. Schiemann, K. Bergmann, and W. S. Warren. Population transfer by stimulated raman scattering with delayed pulses using spectrally broad light. *J. Chem. Phys.*, 96:4215–4223, 1992.

[47] S. Zhdanovich, E. A. Shapiro, M. Shapiro, J. W. Hepburn, and V. Milner. Population transfer between two quantum states by piecewise chirping of femtosecond pulses: Theory and experiment. *Phys. Rev. Lett.*, 100(103004), 2008.

[48] E. Shapiro, V. Milner, C. Menzel-Jones, and M. Shapiro. Piecewise adiabatic passage with a series of femtosecond pulses. *Phys. Rev. Lett.*, 99(033002), 2007.